This is a pre-print which has been accepted for publication in the Journal of Geophysical Reseach: Solid Earth (doi: 10.1029/2022JB023952).

Experimental multiblast craters and ejecta

—

seismo-acoustics, jet characteristics, craters, and ejecta deposits and implications for volcanic explosions

Ingo Sonder[1,*], Alison Graettinger[2], Tracianne B. Neilsen[3], Robin S. Matoza[4], Jacopo Taddeucci[5], Julie Oppenheimer[6], Einat Lev[6], Kae Tsunematsu[7], Greg Waite[8], Greg A. Valentine[1], and Kenneth S. Befus[9]

[1]Center for Geohazards Studies, University at Buffalo, Buffalo, NY, USA
[*]Corresponding author: ingomark@buffalo.edu
[2]Department of Earth & Environmental Sciences, University of Missouri Kansas City, Kansas City, MO, USA
[3]Department of Physics and Astronomy, Brigham Young University, Provo, UT, USA
[4]Department of Earth Science and Earth Research Institute, University of California, Santa Barbara, CA, USA
[5]Istituto Nazionale di Geofisica e Vulcanologia, Rome, Italy
[6]Lamont Doherty Earth Observatory, Columbia University, Palisades, NY, USA
[7]Yamagata University, Yamagata, Japan
[8]Geological and Mining Engineering and Sciences, Michigan Tech, Houghton, MI, USA
[9]Department of Geosciences, Baylor University, Waco, Texas, USA

Key Points

- Airborne energy of an underground blast decays exponentially with scaled depth and is in agreement with previous measurements.

- Transient crater unloading leads to eruption at the surface from depths that were thought to be deep enough to be contained in the ground.
- Crater sizes correlate with measured seismo-acoustic and high-frequency atmospheric signals.

Abstract

Blasting experiments were performed that investigate multiple explosions that occur in quick succession in unconsolidated ground and their effects on host material and atmosphere. Such processes are known to occur during phreatomagmatic eruptions at various depths, lateral locations, and energies. The experiments follow a multi-instrument approach in order to observe phenomena in the atmosphere and in the ground, and measure the respective energy partitioning. The experiments show significant coupling of atmospheric (acoustic)- and ground (seismic) signal over a large range of (scaled) distances (30–330 m, 1–10 m $J^{-1/3}$). The distribution of ejected material strongly depends on the sequence of how the explosions occur. The overall crater sizes are in the expected range of a maximum size for many explosions and a minimum for one explosion at a given lateral location. As previous research showed before, peak atmospheric over-pressure decays exponentially with scaled depth. An exponential decay rate of $\bar{d}_0 = 6.47 \times 10^{-4}$ m $J^{-1/3}$ was measured. At a scaled explosion depth of 4×10^{-3} m $J^{-1/3}$ ca. 1% of the blast energy is responsible for the formation of the atmospheric pressure pulse; at a more shallow scaled depth of 2.75×10^{-3} m $J^{-1/3}$ this ratio lies at ca. 5.5–7.5%. A first order consideration of seismic energy estimates the sum of radiated airborne and seismic energy to be up to 20% of blast energy. Finally, the transient cavity formation during a blast leads to an effectively reduced explosion depth that was determined. Depth reductions of up to 65% were measured.

Plain Language Summary

Blasting experiments using six successive explosions were performed. Explosives were detonated in unconsolidated ground material in four different geometric setups (linear and triangular). We monitored the experiments using geophysical instruments. The instruments measured explosive energy, and how much of that energy escapes the crater. The experiments help to understand volcanic (phreatomagmatic) and other subsurface explosive processes. Exact measurements of the resulting craters, together with known explosive energies allow the interpretation of real volcanic craters. The experimental results show initial time developments of crater sizes, which occurs on the order of one second for crater sizes of the order of one meter. Up to 8% of an explosion's energy was detected as airborne signal. Up to 20% of the explosion's energy was detected as seismic (elastic) energy in the ground.

1 Introduction

Volcanic activity causes subsurface explosions at various depths that can have severe consequences for its environment. Explosions can have several causes, such as interaction of externally derived water in direct contact with magma (Zimanowski, Büttner, et al. 2015) or sudden decompression of a magma column, resulting in the rapid release of dissolved volcanic gases (Cashman et al. 2015). But it is possible to evaluate some of their aspects independent from their cause. A sudden, large pressure change propagates at supersonic speed for a certain distance in a medium such as host rock, magma or atmosphere, causing deformation in elastic, plastic and brittle regimes (e.g. Bowman et al. 2014; Fee et al. 2013; Grady 1996; Kim et al. 2016; Schnurr et al. 2020; Taylor et al. 2010). Shallow explosions fragment and eject magma, host material or both into the atmosphere and pose danger to the surroundings. Deeper explosions (for a given energy release) may be fully contained in the subsurface (Valentine, Graettinger, and Sonder 2014). When an explosion occurs in the subsurface some of energy remains in the ground and some enters the atmosphere. In volcanic settings explosions may occur as individual events or in rapid succession, at various depths and lateral locations. Characterizing the transition from a deeper, fully contained, to a less contained, near-surface explosion is important for assessing both hazards and some principle mechanisms of explosions. Many mechanisms can cause volcanic explosions (Houghton 2015), but some effects on the surroundings are common to all explosive source mechanisms. For example, all explosive processes mix host material. Shallow explosions eject significant amounts of hot material (Graettinger, Valentine, Sonder, Ross, and White 2015). Finally subsurface explosions produce crater structures, that are characteristic for the blast process's energy and location (Valentine, Graettinger, and Sonder 2014).

In natural settings, explosive volcanic blasts and processes are often monitored using multiple techniques including seismic and infrasound observation and video recordings at normal and high speeds (Gaudin et al. 2016; Matoza, Arciniega-Ceballos, et al. 2019). Seismoacoustic studies aim to relate signatures of observed seismic and infrasound waveforms to the source processes generating them. A more controlled process than the poorly constrained natural signals, with known source parameters, can help to constrain uncertainties and enable scalability of models.

An explosion—a sudden, rapid change of a material's volume that it imposes on its surroundings—forces that surrounding medium to rapidly compress such that the resulting pressure change does not propagate with the same speed as a smaller pressure change would. Small pressure changes can be described within the linear acoustic approximation, which assumes small pressure changes from a locally static pressure, and results in waves traveling with a (locally constant) speed of sound. Larger pressure changes cause adiabatic heating in air which locally increases the propagation speed and can lead to dramatic steepening of an initially smooth pressure wave into a discontinuity—a shock (Crighton et al. 1979; Garcés et al. 2013; Muhlestein et al. 2012). In an isentropic approximation (reversible process at constant entropy) a shock pulse has characteristic properties such as amplitude and duration that scale with the explosion's energy and the density of the medium in which the pulse travels (Kinney et al. 1985).

Scaling properties enable the establishment of phenomenological regimes that depend on scaled

parameters, such as a scaled length. For example, for the depth d of a subsurface explosion, a scaled depth can be defined by

$$\bar{d} = \frac{d}{E_{\mathrm{b}}^{1/3}} \quad , \tag{1}$$

where E_{b} is the blast's energy (Holsapple et al. 1980; Sonder, Graettinger, and Valentine 2015). Using this method blasts of any energy may be categorized into deep, intermediate and shallow blasts. Deep blasts are contained in the ground and do not eject material ($\bar{d} \gtrsim 8 \times 10^{-3}\,\mathrm{m\,J^{-1/3}}$). The host material's weight and strength are large enough to "contain" the blasts. Energy is dissipated by friction and anelastic alteration, or transported elastically as seismic waves. At intermediate scaled depths ($\bar{d} \simeq 4 \times 10^{-3}\,\mathrm{m\,J^{-1/3}}$), material is excavated efficiently, which results in the largest craters. Shallow blasts ($\bar{d} < 4 \times 10^{-3}\,\mathrm{m\,J^{-1/3}}$) create a smaller crater. They male smaller craters because more of the blast's energy couple with the atmosphere and fewer with the host, resulting in a large atmospheric pressure pulse. These regimes are backed up by extensive studies from military and mining research (Dillon 1972; Ehrgott et al. 2011; Holsapple et al. 1980; Lee et al. 1989; Qiu et al. 2018), as well as research motivated by volcanology (Ambrosini, Luccioni, et al. 2002; Goto, Taniguchi, et al. 2001; Ross et al. 2013; Sato et al. 1997; Sonder, Graettinger, and Valentine 2015; Valentine, White, et al. 2012). For example, two blasts at same depth, which created craters with radii that differ by a factor 2, had energies that differed by a factor $2^3 = 8$.

Similar phenomenological regimes exist for a blast wave propagating in air. The distance from explosion source, r, may be scaled by blast energy and air density ρ

$$\bar{r} = \frac{\rho\, r}{\rho_0\, E_{\mathrm{b}}^{1/3}} \quad . \tag{2}$$

The reference density ρ_0 is a value known from a case for which the scaled distance is known. Similar to $\bar{d}$, $\bar{r}$ may be used to categorize an observation distance into far ($\bar{r} \gtrsim 6 \times 10^{-2}\,\mathrm{m\,J^{-1/3}}$), in which the peak pressure drops with $\bar{r}^{-1}$, intermediate ($\bar{r} \simeq 6 \times 10^{-3}\,\mathrm{m\,J^{-1/3}}$), or near ($\bar{r} \lesssim 10^{-3}\,\mathrm{m\,J^{-1/3}}$), (Kinney et al. (1985)).

Less studied, from a volcanological perspective, are the effects of scaled depth on monitoring signals such as seismic, acoustic, and infrasound, particularly in cases involving multiple explosions occurring in rapid succession. Crater structures and ejecta products of such blasts are analyzed, and allow to connect their geometries and stratigraphy to energy, explosion locations and sequencing. These field findings also reveal the complexities of the natural processes, which limit the straight forward application of simple explosion models (Taddeucci, Sottili, et al. 2010). Some factors controlling the dynamic behavior and energy scaling have a common base with other applications of explosives in the fields of military or mining research (Ambrosini and Luccioni 2006; Qiu et al. 2018). Such applications allow the scaling of lengths with a blast's energy, and use the depth below the surface to quantify its confinement. The scaling relationships were found experimentally, and while in detail the phenomena associated with a subsurface explosion depends on factors such as a host material's strength and density, rough phenomenological regimes can be identified that are primarily related to energy and depth combinations. Energy scaling was experimentally verified across length

scales ranging from 10^{-2} m to 10^{3} m, and energies from 10^{3} J to 10^{15} J (Sato et al. 1997; Strange et al. 1960; Vortman 1968). Energies of most volcanic blasts fall into this range (Valentine, Graettinger, and Sonder 2014), and experimental research suggests that decompression driven blasting results in a similar scaled crater radius to depth relationship, even though changes in absolute values may have to be made, due to the different characteristics of the energy source (Liu et al. 2020). This motivates either direct applicability of the methods or a version adapted to volcanic activity.

Here we report results of experiments that focus on the effects of multiple explosions, closely spaced and timed, on ejecta, crater morphology, and geophysical signals. Such explosions show different behavior depending on the state of topography and host conditions at the time of explosion. Both conditions are varying rapidly, which causes ejecta jets to become asymmetric (Figure 1, supporting video S1–S8), and can also be observed in the field on the volcanic scale (Voight 1981). A volcanic explosive source was replaced by time- and energy-constrained chemical explosions. Previous experimental studies showed that this approach has important implications for field-scale analysis and interpretation (Bowman et al. 2014; Goto, Taniguchi, et al. 2001; Graettinger, Valentine, Sonder, Ross, and White 2015; Graettinger, Valentine, Sonder, Ross, White, and Taddeucci 2014; Graettinger, Valentine, and Sonder 2015; Macorps et al. 2016; Sato et al. 1997; Sonder, Graettinger, and Valentine 2015; Valentine, Graettinger, Macorps, et al. 2015; Valentine, Graettinger, and Sonder 2014). In these previous experiments explosive charges were detonated separately, and the effects of each single detonation on the surface morphology and ejected material were studied before detonating the next charge. Although that approach is relevant to many volcanic settings, observation shows that during explosive eruptions many explosions can occur closely spaced in time (Matoza, Fee, et al. 2014; Park et al. 2021) or simultaneously, superposing their tephra jets, to create one single cumulative eruption column (Dürig, M. Gudmundsson, et al. 2015). Our study tests whether the results of previous experiments with separate blasts can be extended to those with blasts in rapid succession and with lateral and vertical migration.

2 Experimental Setup & Methods, Data Interpretation

2.1 Experiments

For each of the experiments reported here six charges were buried and detonated in test pads which were filled with unconsolidated granular material. The setup roughly follows previous studies on craters, each of which was created by more than one explosion ("multiblast craters") in which charges were detonated, and their blasts studied one at a time (Graettinger, Valentine, Sonder, Ross, White, and Taddeucci 2014; Sonder, Graettinger, and Valentine 2015; Valentine, White, et al. 2012). The use of unconsolidated granular material as host is motivated by the focus on the effects of multiple explosions. We note that any natural occurring rock material looses strength with scale (e.g. Hoek 1999). Specifically in volcanic environments host material tends to be fractured. The presented experiments do not aim to determine the difference to blasting in solid rock material. The explosive material was Pentex™, which is a proprietary compound material with major components including trinitrotoluene (TNT) and pentaerythritol (PETN). It has a specific energy of $4.85 \times 10^{6}\,\mathrm{J\,kg^{-1}}$;

Figure 1: Side- and top view of a typical asymmetric ejecta jet created by the detonation sequences. Red markers show the pre-blast surface above explosive charges. The example shows the jet of the third detonation in the "pad 1" configuration. Location markers for the third charge are bold. (See also supporting videos S1 and S5.)

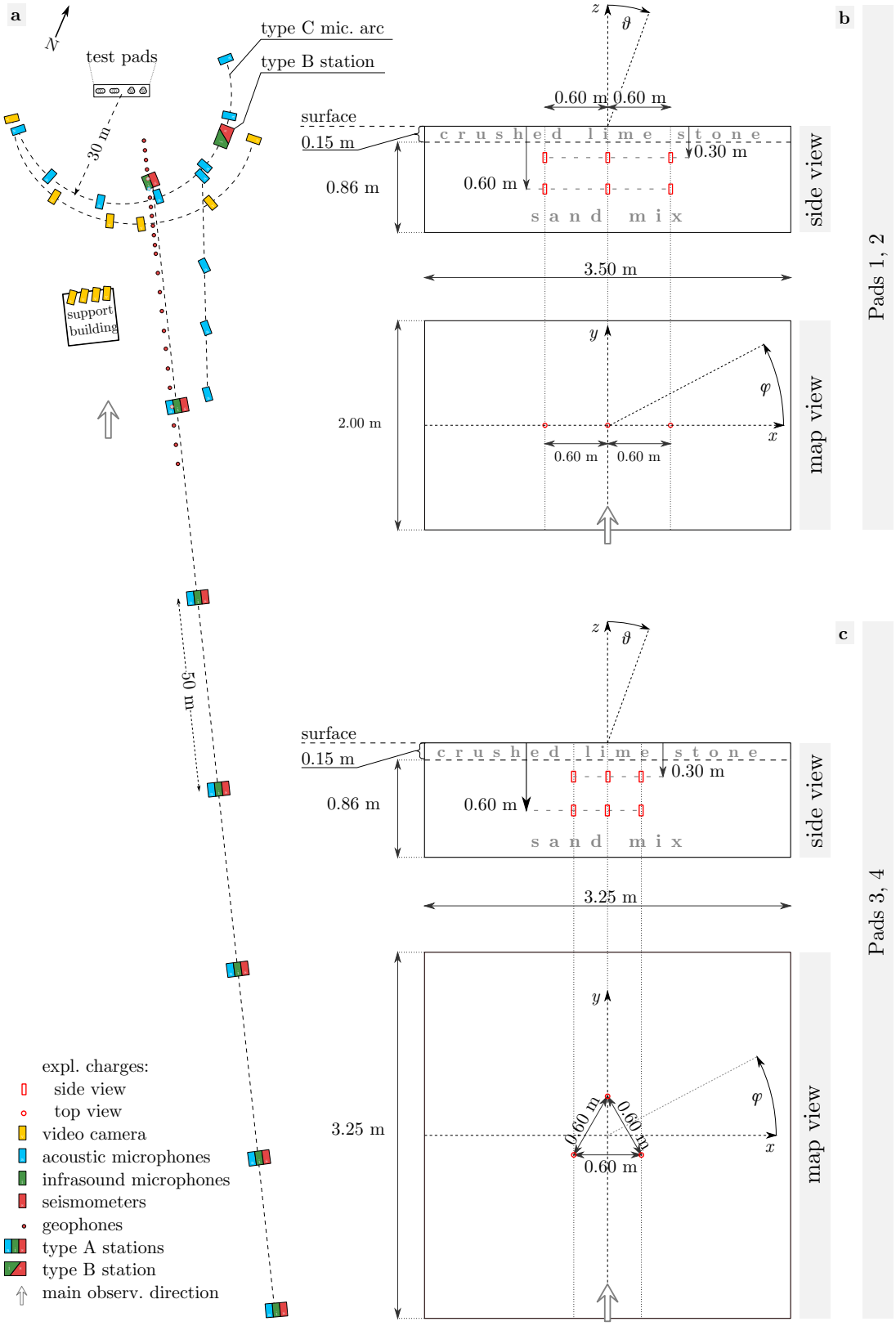

Figure 2: (*Caption on next page*)

Figure 2: Multi-sensor stations were placed in a radial line every 50 m starting at 30 m distance from the test pads. Each station included compact broadband seismic and infrasonic sensors as well as broadband ("acoustic") microphones. Acoustic microphones were placed in a 30 m radius semicircle around the center of the test pads. Another set of microphones was placed in a radial line from the test pads ranging from 30 m to 80 m. 12 geophones were placed every 2.5 m starting at 12 m from the pads center, and 11 more along the same direction every 5 m following that. The last geophone had a distance of 99.5 m from the pads center. Six identical cameras recorded the experiments also in an arc of about 30 m distance. Other cameras recorded from a 50 m location.

---

each charge had a mass of 90 g which corresponds to an energy of 4.37×10^5 J. The six charges were detonated in a timed sequence of 0.5 s between each detonation. Accuracy of detonation timing was better than 10^{-3} s. This timing was selected to ensure that the ejecta jet of each blast interacted with that of the preceding blast. Two plan-view configurations were set up; one with three charge epicenters in a line (Figure 2b); another with three epicenters corresponding to the apexes of a triangle (Figure 2c). Charges were arranged vertically on top of one another, at two depths, 30 cm and 60 cm. At the given blast energy 30 cm corresponds to a scaled explosion depth of $3.95 \times 10^{-3}\,\mathrm{m\,J^{-1/3}}$, a value very close to optimum excavation conditions. Horizontal spacing was chosen, such that the horizontal neighbor charge location would be within the footprint of a single blast at optimum depth, but close to its border. At pads 1 and 3 the upper charges were detonated in sequence, followed by the three lower charges. At pads 2 and 4, charges beneath each epicenter were detonated in a sequence of shallow-first and deeper-second (Figure 3).

The blast sequences were monitored by high-speed and normal speed video cameras deployed on ground and on unoccupied areal vehicles (UAVs). A set of six cameras was arranged in a hemicycle, at a distance between 20–30 m to accurately capture directions of ejected materials. UAV-based video was recorded to determine lateral jet directions and material motion. High-speed cameras recorded at 300, 500 and 5000 fps.

Seismo-acoustic records were made using a combination of seismometers, geophones, infrasound-microphones ("infrasound sensors") and higher frequency broadband microphones ("acoustic microphones"). The deployed seismometers and infrasound sensors fit into the SEED broadband category (band code "C", Ahern et al. 2012). Seismometers and infrasound sensors were recorded at 400 Hz or 500 Hz. Deployed infrasound sensors had a flat frequency response between 3×10^{-2} Hz and Nyquist frequency. Two types of the acoustic microphones were used, with linear (±2 dB) response from 3.15 Hz to 20 kHz and 4 Hz to 80 kHz (Table 1). Despite the familiar name "acoustic microphones" these sensors range far into the ultrasonic range. Recordings in this frequency range are rare for volcano seismo-acoustics, which often end around 5 kHz Nyquist (Taddeucci, Peña Fernández, et al. 2021). Some existing high-frequency field scale recordings are available from Goto, Ripepe, et al. (2014) and Yokoo et al. (2002) who sampled at up to 50 kHz, and Ichihara et al. (2009), who report recordings at 200 kHz sampling rate.

From these sensors seismo-acoustic measurement stations were assembled for specific purposes. Station type A was dedicated to measure the radial decay of airborne- and ground-based blast signals. For each of the type A stations a 3-component seismometer, an infrasound microphone and

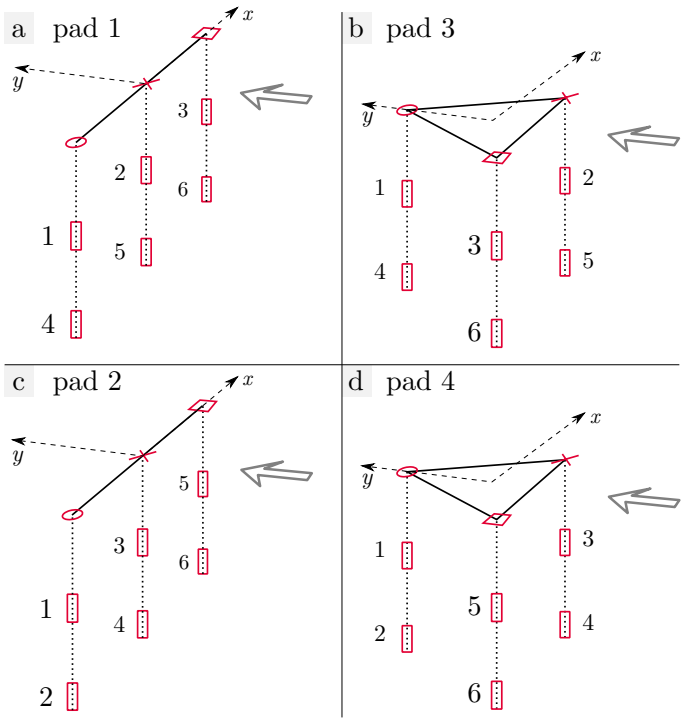

Figure 3: Firing sequence of the four test pads. Numbers indicate the position of the firing sequence.. Charges were fired at 0.5 s intervals. **a, b**: In pads 1 and 3 the upper charges (buried at 30 cm depth) were the first three to be fired, before the lower level (buried at 60 cm depth) was fired in the same lateral sequence as the upper ones. **c, d**: In pads 2 and 4 charge pairs located at same horizontal location were fired consecutively (upper level before lower level). The main observation direction is shown by the large, gray arrow. The origin of the crater-specific calculations is set to pre-blast surface level for the vertical coordinate (z), and the geometric center of the charges (centroid) for the lateral coordinates (x, y indicated as dashed lines). Markers at the surface level show the 'epicenters' above the charges. A circle shows epicenters above the first fired charge, a square shows an epicenter above the last fired charge, and a cross shows the epicenter above the in-between fired charges.

two acoustic microphones were used. The seismometer was placed 1 m below the ground surface, and the infrasound sensor was just below the surface. The microphones were mounted 4 m above ground, pointing towards the blast source, and just above ground, pointing downwards. Seven type A stations were placed every 50 m in a radial line, starting at 30 m distance from the test pads center, so that the last station was at 380 m distance (Figure 2). Station type B was dedicated to the depth dependency of blast signals. One station was assembled which consisted of three 3-component seismometers, placed 132 cm, 75 cm and 18 cm below the surface, and one infrasound sensor, placed just below the surface. Station B had a distance of 30 m from the blast pads center (Figure 2). Station type C was dedicated to measure the angular dependency of the airborne signals. For each of them two acoustic microphones were placed 2.44 m and 1.22 m above ground. Type C stations were placed in a 30 m radius semi-circle around the center of the blast pads. Angles range from 0°to 180° and were arranged so that the 90° station was also the start of the type A radial line (Figure 2). Seismo-acoustic setup also included a line of 23 geophones to record ground speeds at 12 m–100 m distance along the type A radial line.

Ejected material was collected in two box arrays, separated at an angle $> 45°$ to collect material from 2.5–13.5 m from the charge assembly's center. The sample arrays were re-positioned for each experiment, so that they were always centered around an explosion site. One array was typically at an angle $\varphi = 90°$. The other array had different orientations for each pad, because other equipment and arrangements restricted the available space.

After the charges had detonated and ejecta jets had dissipated, photographs of the produced compound craters were taken for photogrammetry (structure-from-motion) analysis. Photographs were taken using (a) the same UAVs that also recorded blast videos, and (b) using a standard SLR camera, operated by a ground-based person. A subset of the photographs was the base for digital elevation models (DEMs) that were created using the commercial photogrammetry software Metashape™, generally following previous experiments (Graettinger, Valentine, and Sonder 2015). The resulting DEMs have a spatial resolution between 1 cm and 1.5 cm for pads 1–3, and 2.5 cm for pad 4. All crater profiles- and sizes presented below are based on these elevation models.

2.2 Previous Work Used for Analysis

2.2.1 Seismo-Acoustics

An explosion is a sudden volume increase of a substance ('the explosive'), often caused by a highly exothermal chemical reaction. The expansion rate is larger than the speed of sound of the surrounding material which, in a general case, may be solid, liquid or a gas. The process compresses its environment faster than the latter can transport (at the speed of sound), which causes an over-steepening of the related pressure pulse and eventually produces a pressure disconituity ('jump'). Close to the source the pressure jumps from ambient (atmospheric) value to a maximum and then relaxes back before sinking below ambient pressure and again relaxing back. At larger distances the propagation speed approaches the speed of sound and the pressure discontinuity relaxes to a steep, but finite slope.

Using features of wave-forms recorded by microphones and/or seismic sensors it is possible to

Table 1: Sensor setup of the three seismo-acoustic station types.

Station Type *Dependency* Deployment	Sensors Per Station[1]	Vertical Setting (Direction)[2]	Sampling Rate	Frequency Range (± 2 dB)[3]	Remarks
type A *radial* 7 stations	seismometer	-1 m	400 Hz		Nanometrics 120s Trillium Compact Posthole
	infrasound	0 m		0.03 Hz $-$200 Hz	Chaparral Model 60 UHP
	microphone 1	$+4$ m (towards blast)	204.8 kHz	3.15 Hz $-$ 20 kHz	1/2" pre-polarized GRAS 40AE, 40AO
	microphone 2	$+0.1$ m (towards gnd.)			
type B *depth* 1 station	seismometer 1	-0.18 m	500 Hz		Guralp CMG3ESP 60sec
	seismometer 2	-0.75 m			
	seismometer 3	-1.32 m			
	infrasound	-0.05 m		0.03 Hz $-$ 250 Hz	Honeywell Differential Pressure Sensor
type C *angular* 6 stations	microphone 1	$+2.44$ m	204.8 kHz	4 Hz $-$ 80 kHz	1/4" pre-polarized GRASS 40BE
	microphone 2	$+1.22$ m			

[1]: Each seismometer in any of the stations had three components, North ('N' or '1'), East ('E' or '2') and vertical ('Z'). Components were aligned vertically (positive downward, 'Z'), radially (positive pointing away from the direction of the blast source, 'N', '1'→'R') and to the transverse direction (perpendicular to radial, 'E' or '2'→'T').

[2]: Vertical distance relative to local ground surface: positive above, negative below. Direction in parentheses is the direction of the microphone maximum sensitivity.

[3]: Upper limit refers either to Nyquist frequency or to sensor limit, see text. The ± 1 dB frequency range of the 40 AE, 40 AO is 5 Hz $-$ 10 kHz; frequency range of the 40 BE is 10 Hz $-$ 40 kHz.

estimate the blast's energy, provided that scaling laws assumed in such models are valid. The scaled peak pressure and scaled impulse of a blast in air depends on the scaled distance where the pressure is measured (Kinney et al. 1985). This relationship can be used to determine the scaled distance of each microphone record, and with that the energy of each blast wave can be estimated. This resource will be used as a reference model, and referred to as KG85 data (or -model). For these blasts in air, the main fundamental three quantities to be scaled are distance, time, and pressure. As in the case for underground blasts distances can be scaled with blast energy E_b. Additionally, the relatively high atmospheric homogeneity allow further specification of the atmospheric density, which is often written in terms of transmission factors for scaled distance and time. Scaled distance, time, and pressure are given by

$$\bar{r} = \frac{f_d\, r}{E^{1/3}} \quad , \quad \bar{t} = \frac{f_t\, t}{E^{1/3}} \quad , \quad \bar{p} = \frac{p}{p_\mathrm{a}} \quad , \tag{3}$$

where p_a is the atmospheric pressure and the transmission factors f_d, f_t for distance and time, respectively, take the density into account in which the blast pulse propagates. They are given by

$$f_d = \left(\frac{\rho}{\rho_0}\right)^{1/3} = \left(\frac{p_\mathrm{a} T_0}{p_0\, T}\right)^{1/3} \quad , \quad f_t = \left(\frac{\rho}{\rho_0}\right)^{1/3} \frac{c}{c_0} = \left(\frac{p_\mathrm{a}}{p_0}\right)^{1/3} \left(\frac{T}{T_0}\right)^{1/6} \quad . \tag{4}$$

Here, T is temperature and index $_0$ refers to values of a known blast case. The model only applies to explosive shocks in air. Energy E in Equation 3 refers to the blast's energy, E_b, and assumes that the blast wave did not pass any material boundary. In case of subsurface blasts this value has to be reduced, since part of E_b is dissipated and transported in the ground. If enough energy is not contained in the ground this part, E_a, creates a (smaller) shock pulse in the atmosphere. Measurement of E_a is described in section 3.3.1.

Another widely used quantity to measure a blast's intensity, damage potential and energy is its impulse per cross-sectional area (Bush et al. 1946; Guzas et al. 2010; Kinney et al. 1985; Schnurr et al. 2020), which can be obtained as the time integral of the initial positive pressure peak of a microphone pressure curve as

$$I_1 = \int_{t_\mathrm{s}}^{t_1} p\, dt \quad . \tag{5}$$

Here t_s is the start time (time of arrival of the pulse at the sensor's location) and t_1 is the time of first zero crossing of the pressure curve (Figure 6). This time interval always contains the peak pressure. The corresponding scaled impulse is a compound of scaled pressure and time components

$$\bar{I}_1 = \int_{\bar{t}_\mathrm{s}}^{\bar{t}_1} \bar{p}\, d\bar{t} = \frac{f_t}{p_\mathrm{a}\, E_\mathrm{a}^{1/3}}\, I_1 \quad . \tag{6}$$

The KG85 data provides values up to a scaled distance of $3.1\,\mathrm{m\,J^{-1/3}}$ ($500\,\mathrm{m\,kg^{-1/3}}$). According to this dataset the scaled pressure and scaled impulse decay with $1/\bar{r}$ at relatively large distances

($\bar{r} \gtrsim 10^{-1}\,\mathrm{m\,J^{-1/3}}$, $20\,\mathrm{m\,kg^{-1/3}}$). The explicit values for the decay are

$$\bar{p} = \frac{a_{p,\mathrm{ref}}}{\bar{r}} \quad , \quad a_{p,\mathrm{ref}} = 5.135 \times 10^{-3}\,\mathrm{m\,J^{-1/3}} \quad , \tag{7}$$

$$\bar{I}_1 = \frac{a_{I,\mathrm{ref}}}{\bar{r}} \quad , \quad a_{I,\mathrm{ref}} = 5.923 \times 10^{-8}\,\mathrm{m\,s\,J^{-2/3}} \quad . \tag{8}$$

As is common in the analysis of blast waves (Garces 2018; Kinney et al. 1985), peak pressures were not directly read as the maximum of the measured pressure curve, but impulse I_1 was calculated and compared to a function representing a blast pulse shape. We used a modified Friedlander shape $\bar{p}(t) = \bar{p}_\mathrm{p}\,(1 - \frac{t-t_\mathrm{s}}{t_1-t_\mathrm{s}})\,\exp(-\alpha\frac{t-t_\mathrm{s}}{t_1-t_\mathrm{s}})$, see e.g. Marchetti et al. (2013). Here $\bar{p}_\mathrm{p}$ is the scaled peak pressure, and α is a positive number that determines the strength of the exponential's decay. The value of p_p that fits the measured I_1 best was used for the peak overpressure. The impulse reference data are somewhat unclear, because the reference interpolation function (Equation 29) deviates from the reference data points by 17%. Since both, interpolation function and data points are part of the same publication (Kinney et al. 1985), we decided to follow their measured data instead of their interpolation parameter. Therefore one parameter of the interpolation function was adjusted, the constant $\bar{I}_0$ in Equation 29, which provides a better fit. Interpolation formulas, an explicit listing of all interpolation parameters and a graph that shows the difference between the two values of $\bar{I}_0$ are given in B, Table 5 and Figure 15, respectively.

Ford et al. (2014) determined distance- and depth-dependent energy partitioning of explosions above and below ground using a model for the airborne signal that, after some re-formulation (C), can be written as

$$\bar{I}_1 = \frac{b_1}{\bar{r}} \frac{e^{-\bar{d}/\bar{d}_3}}{\left(1 + e^{-10\bar{d}/\bar{d}_3}\right)^{1/10}} \quad . \tag{9}$$

Here $b_1 = 1.15 \times 10^{-7}\,\mathrm{s\,m\,J^{-2/3}}$ and $\bar{d}_3 = 1.2 \times 10^{-3}\,\mathrm{m\,J^{-1/3}}$. Evaluated at $\bar{d}$ =0 this model expects a ca. 7% smaller scaled impulse (factor $2^{-1/10}$, $\simeq 0.93$) at a given distance compared to a free air blast. A larger discrepancy exists with respect to the KG85 data: The two constants for the $\bar{r}^{-1}$ dependency, $a_{I,\mathrm{ref}}$, and b_1 differ by a factor 0.51. Detemination of E_a from the scaled radial to scaled impulse relationship, as done in section 3.3.1 (Equation 15) using b_1 instead of $a_{I,\mathrm{ref}}$ yields a factor $(a_{I,\mathrm{ref}}/b_1)^{3/2} \simeq 0.37$ reduced values for E_a. The dataset presented here does not contain a zero depth or free air blast, and therefore cannot decide for one of the models. Energy values listed in Table 3 used the KG85 constant, and should be adjusted if used in connection with Equation 9.

Equation 9 and microphone records of previous blast sessions, carried out in very similar host materials and with similar explosives, show that scaled impulse decays rapidly with scaled depth (A). A somewhat more accurate match with experimental data is obtained for the peak pressure dependency on depth. Therefore the following is formulated using a peak pressure dependency. At depths $\bar{d} < 5 \times 10^{-3}\,\mathrm{m\,J^{-1/3}}$ peak pressure can be approximated by a product of an exponential which contains the depth part and an amplitude containing the radial dependency:

$$p_\mathrm{p} = A(\bar{r})\,e^{-\bar{d}/\bar{d}_0} \tag{10}$$

Here the scaled depth related constant $\bar{d}_0 = 5.4 \times 10^{-4}\,\mathrm{m\,J^{-1/3}}$. This approximation is valid for scaled depths smaller than $5 \times 10^{-3}\,\mathrm{m\,J^{-1/3}}$ (Figure 14).

2.2.2 Energy Scaling and Crater Morphology

As described above, the scaled radius of a single sub-surface blast depends on the scaled depth of explosion. At several places, below analysis relies on a functional relationship of the two scaled values. Sonder, Graettinger, and Valentine (2015) published an empirical function that uses understandable parameters for this dependency:

$$\bar{r}_1(\bar{d}) = \begin{cases} (\bar{r}_{\max} - \bar{r}_0)\left(\dfrac{\bar{d}}{\bar{d}_{\mathrm{opt}}} - 1\right)^2 + \bar{r}_{\max} & \text{if } \bar{d} \le \bar{d}_{\mathrm{opt}} \\ \dfrac{\bar{r}_{\max}}{\sqrt{1 + \left((\bar{d} - \bar{d}_{\mathrm{opt}})\dfrac{\bar{r}_{\max}}{b}\right)^2}} & \text{if } \bar{d} \ge \bar{d}_{\mathrm{opt}} \end{cases} \tag{11}$$

The subscript $_1$ of this radius refers to the first blast in a sequence. The meaning of the four parameters is: $\bar{d}_{\mathrm{opt}}$ is the 'optimal' scaled depth of explosion; the scaled depth that crates the largest scaled crater of radius $\bar{r}_{\max}$. $\bar{r}_0$ is the scaled crater radius an explosion creates at 0 scaled depth. And b is a decay constant that determines how strong radius decreases with scaled depth at depths larger than $\bar{d}_{\mathrm{opt}}$. The values used for these parameters reflect the combination of unconsolidated host material and explosive charges, which were the same for Sonder, Graettinger, and Valentine (2015) and the here presented experiments. Values used for Equation 11 are $\bar{d}_{\mathrm{opt}} = 3.85 \times 10^{-3}\,\mathrm{m\,J^{-1/3}}$, $\bar{r}_{\max} = 7.51 \times 10^{-3}\,\mathrm{m\,J^{-1/3}}$, $\bar{r}_0 = 2.38 \times 10^{-3}\,\mathrm{m\,J^{-1/3}}$ and $b = 1.72 \times 10^{-5}\,\mathrm{m^2\,J^{-2/3}}$.

There is an upper limit for the size of a crater structure (volume or radius) which is created by a sequence of a (potentially) unlimited number of explosions at the same lateral location. Despite the (potentially) unlimited cumulative energy spent by the explosions, any *single* explosion can only break up finite amounts of material and eject material to a finite distance, thereby creating a "multi-blast crater" of finite size. The upper limit of a crater's size, for example given by its radius, r_∞, is the balance between amount of ejected material by an explosion and the amount of material falling back into the crater directly and collapsing from the crater walls. Quantifying the behavior from the first explosion in undisturbed ground to many explosions, Sonder, Graettinger, and Valentine (2015) showed that the change of scaled crater size decreases with increase in the number of explosions

$$n_0 \frac{d\bar{r}}{dn} = \bar{r}_\infty - \bar{r} \quad , \tag{12}$$

where the independent variable n is the number of blasts that occurred, and $n_0 = 0.9$ is a constant, which was determined from experiments. n can be expressed as the ratio of total (cumulative) blast energy of a sequence to single blast energy $n = E_{\mathrm{b,tot}}/E_{\mathrm{b}}$, which is useful in cases of changing scaled depths or E_{b}, so that n may assume non-integer values. For a sequence that starts from zero crater

radius, Equation 12 has the solution

$$\bar{r} = \bar{r}_\infty \left(1 - e^{-n/n_0}\right) \quad , \tag{13}$$

where $n_0 = 0.9$ is an experimentally determined constant. We note that, because of the exponential asymptotic and $n_0 < 1$, $\bar{r}$ approaches $\bar{r}_\infty$ already for $n = 3$ or 4.

In subsurface blasting the depth of explosion (depth of burial) is usually measured as the distance to the horizontal surface. For volcanic applications most explosions occur in- or under a crater or under existing, non-flat topography, which removes the reference level from which depth was determined. Experimental investigation showed that in a first approximation, the shortest distance to the surface can be used as reference level (e.g. Valentine, White, et al. 2012). For the case that an explosion occurs under the center of a crater, the crater bottom is the appropriate first-order approximation to measure the explosion depth. Taking into account the crater shape Sonder, Graettinger, and Valentine (2015) showed that the mass distribution above the charge imposes a 'confining force', and an 'effective depth' can be defined from a crater's topography that reduces the scatter in crater size measurements. The study also showed that the effective explosion depth rarely deviates by more than 10–20% from the closest point to the surface.

3 Observations and Results

3.1 General Observations

For all pads, the initial blast transported the greatest mass of material. From the main observation direction this charge was located at the top-left end of the linear setups of pads 1 and 2, and at the top-rear corner of the triangular setups of pads 3 and 4 (Figure 3). Size and speed of these initial blasts (jets) had a range of 15–25 m, and speeds of several $10\,\mathrm{m\,s^{-1}}$ away from the ground. The initial ground motion exceeded $100\,\mathrm{m\,s^{-1}}$. These values are comparable to previously conducted experiments (e.g. Graettinger, Valentine, Sonder, Ross, and White 2015; Valentine, White, et al. 2012). Ejecta jets of the quieter blasts showed similar thinning behavior as was observed in previous experiments for blasts under pre-existing crater-topography (Graettinger, Valentine, Sonder, Ross, and White 2015; Ross et al. 2013). Some jets had a main direction that was not vertical, but had a certain direction towards the main (temporally changing) crater void showing similarities with previously conducted off-center blast experiments (Valentine, Graettinger, Macorps, et al. 2015). For pads 2 and 4, for which the lower charges were fired only 0.5 s after the upper charge (at same lateral location), the perceived loudness (not measured amplitude) of these lower charges was significantly larger compared to the previous optimum depth blast. In contrast, for pads 1 and 3, for which lower charges were fired 1.5 s after the upper charge at same lateral location, the blast noise was significantly muffled (Table 2).

Table 2: Qualitative comparison of blast experiment configuration and resulting noise and direction. The "left" and "right" labels refer to the jet directions as seen from the main observation location. Polar- and inclination angles are also illustrated in Figure 2b and c.

pad	blast	depth	delay after 1st chrg.	delay after corresp. chrg.[1]	perceived loudness	Inclination (θ)	approx. polar angle (φ) [2]
1	1	30 cm	0 s	0 s	medium	none	–
	2	30 cm	0.5 s	0 s	medium	$> 30°$	180° (left)
	3	30 cm	1 s	0 s	medium	$> 30°$	180° (left)
	4	60 cm	1.5 s	1.5 s	muffled	none	0° (–)
	5	60 cm	2 s	1.5 s	muffled	$> 30°$	180° (left)
	6	60 cm	2.5 s	1.5 s	muffled	$> 30°$	180° (left)
2	1	30 cm	0 s	0 s	medium	none	–
	2	60 cm	0.5 s	0.5 s	loud	none	–
	3	30 cm	1 s	0 s	medium	$> 30°$	180° (left)
	4	60 cm	1.5 s	0.5 s	loud	$> 30°$	180° (left)
	5	30 cm	2 s	0 s	muffled	$> 30°$	180° (left)
	6	60 cm	2.5 s	0.5 s	loud	$\lesssim 20°$	95° (left)
3	1	30 cm	0 s	0 s	medium	none	–
	2	30 cm	0.5 s	0 s	medium	medium	135° (left)
	3	30 cm	1 s	0 s	medium	large	30° (right)
	4	60 cm	1.5 s	1.5 s	muffled	low	270° (–)
	5	60 cm	2 s	1.5 s	muffled	medium	150° (left)
	6	60 cm	2.5 s	1.5 s	muffled	large	30° (right)
4	1	30 cm	0 s	0 s	medium	none	–
	2	60 cm	0.5 s	0.5 s	loud	none	–
	3	30 cm	1 s	0 s	medium	medium	135° (left)
	4	60 cm	1.5 s	0.5 s	loud	low	135° (left)
	5	30 cm	2 s	0 s	medium	medium	<30° (right)
	6	60 cm	2.5 s	0.5 s	loud	low	<30° (right)

[1]: Delay of the lower charges, relative to the upper charge at same lateral location (cf. Figure 3).

[2]: Polar angle is counted counter clock wise, and 0° along the axis parallel to the charge lines of pads 1 and 2, pointing to the right as seen from main observation direction.

3.2 Jets, Craters and Ejecta

Unlike past experiments in which a crater was analyzed after each individual blast, the timing of these multiblast experiments only allows for inspection of the final crater and ejecta. This crater is the cumulative product of six blasts that migrate vertically and laterally through the host. The blast sequences in pads 1 and 2 created craters elongated along the axis of the charges. The final craters of the triangular blast sequences (pads 3 and 4) were more round, with some visibility of single-charge crater outlines in the triangle's corners (Figure 4).

The deepest points of the pad 1 and pad 2 craters were located between the central and right charge positions in the x-direction, and in close proximity to the symmetry line along the charges in y-direction. The lower right charge was always the last to detonate. The crater profiles preserved a stepped floor centered over the final charge (Figure 4). The ejecta showed a prominent ray (ridge of material) that extended from the final charge location out of the crater in the direction of elongation ($\varphi = 180°$). Parts of the ray could be traced more than 10 m from the crater. For pad 1, one of the ejecta sample arrays was in line with this ray (supplementary video S1); in this direction the ejected mass per area was a factor $\simeq 10$ higher compared to the material collected by the array perpendicular to the charge line (Figure 5). Also, mass distribution is better described by an exponential distribution in the $\varphi = 180°$-direction compared to the 90°-direction which is better approximated by a power law. Isolated pieces of shallow-sourced gravel from pads 1 and 2 were observed further from the charges; one of them over 30 m away from pad 2, in the $\varphi = 180°$-direction.

The asymmetry of ejecta distribution around the linear charge array is similar to what was observed in previous off-center multiblast configurations with temporally well separated charge detonations (Valentine, Graettinger, Macorps, et al. 2015). However, in those experiments a steep ejecta ring was formed on the side of the crater opposite to the direction of jet inclination (Graettinger, Valentine, and Sonder 2015). This steep ejecta rim was not observed in the here presented, overlapping blast sequences.

The triangular blast sequences of pads 3 and 4 produced more equant crater shapes resembling blurred circles around the triangular blast centers (Figure 4). Compared to the linear setups the deepest points of the craters were located laterally closer to the centroid and had a larger distance to the last blast's center. The pad 3 crater had a low point between the first and second (lateral) blast locations. Pad 4 had the low point close to its centroid. Both of the craters had shallow slopes in the vicinity of the crater rim (the topographic high around a crater center). Slopes were steeper closer to the center of craters. Ejecta were concentrated in three main directions for pad 3, and two for pad 4. Compared to the linear charge setups, the observed ejecta concentrations of the triangular sequences were less pronounced. The ejecta concentrations originate from one vertex of the charge configuration to bisect the opposite side of the triangle (supporting video S3). The pad 3 sequence had ejecta concentrations correlating to all three lateral charge positions. In the pad 4 sequence ejecta rays only correlated to blasts 3, 4 ($\varphi \simeq 150°$) and 5, 6 ($\varphi \simeq 30°$), since the first two blasts occurred in an effectively radially symmetric setting (blast 1 under flat topography, blast 2 under an approximately radially symmetric transient cavity).

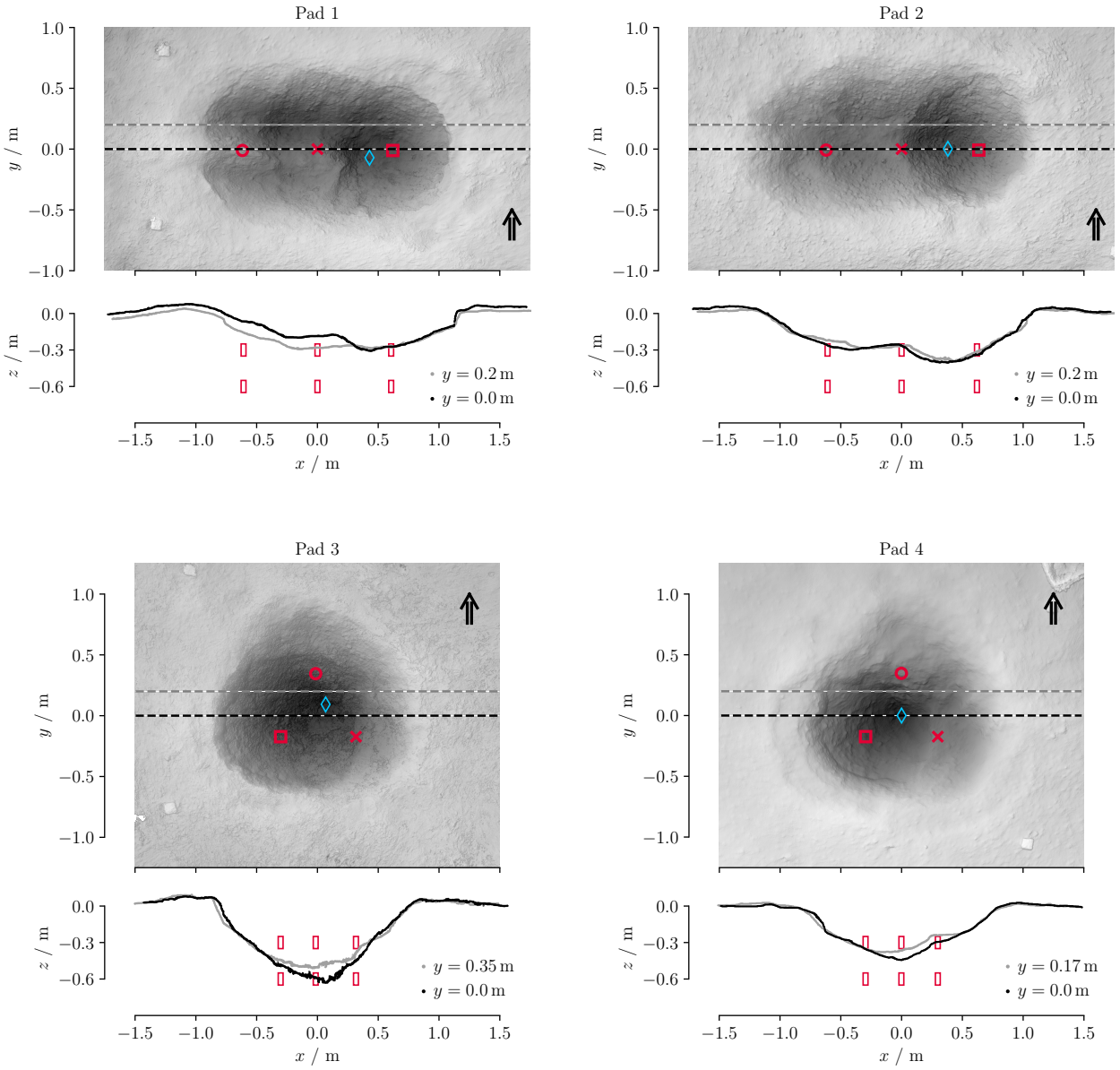

Figure 4: Map view and selected crater profiles of the crater structures. Red markers in the map view mark locations of the first (cross), intermediate (square), and the last (circle) charge fired. For clarity, squares for intermediate charges at first and last locations were omitted. Blue diamonds show the deepest points of the craters. The main observation direction was parallel to the y-coordinate (black arrows). Red boxes in the profile views show vertical charge locations. The pre-blast surface was at $z = 0$. The linear charge arrangements (pads 1 and 2) created a stepped profile that reflect the blast history to some extent. Their deepest point was about 30 cm, the upper charge depth. Sequences shot in the triangular geometries (pads 3 and 4) excavated significant amounts of material from below 30 cm.

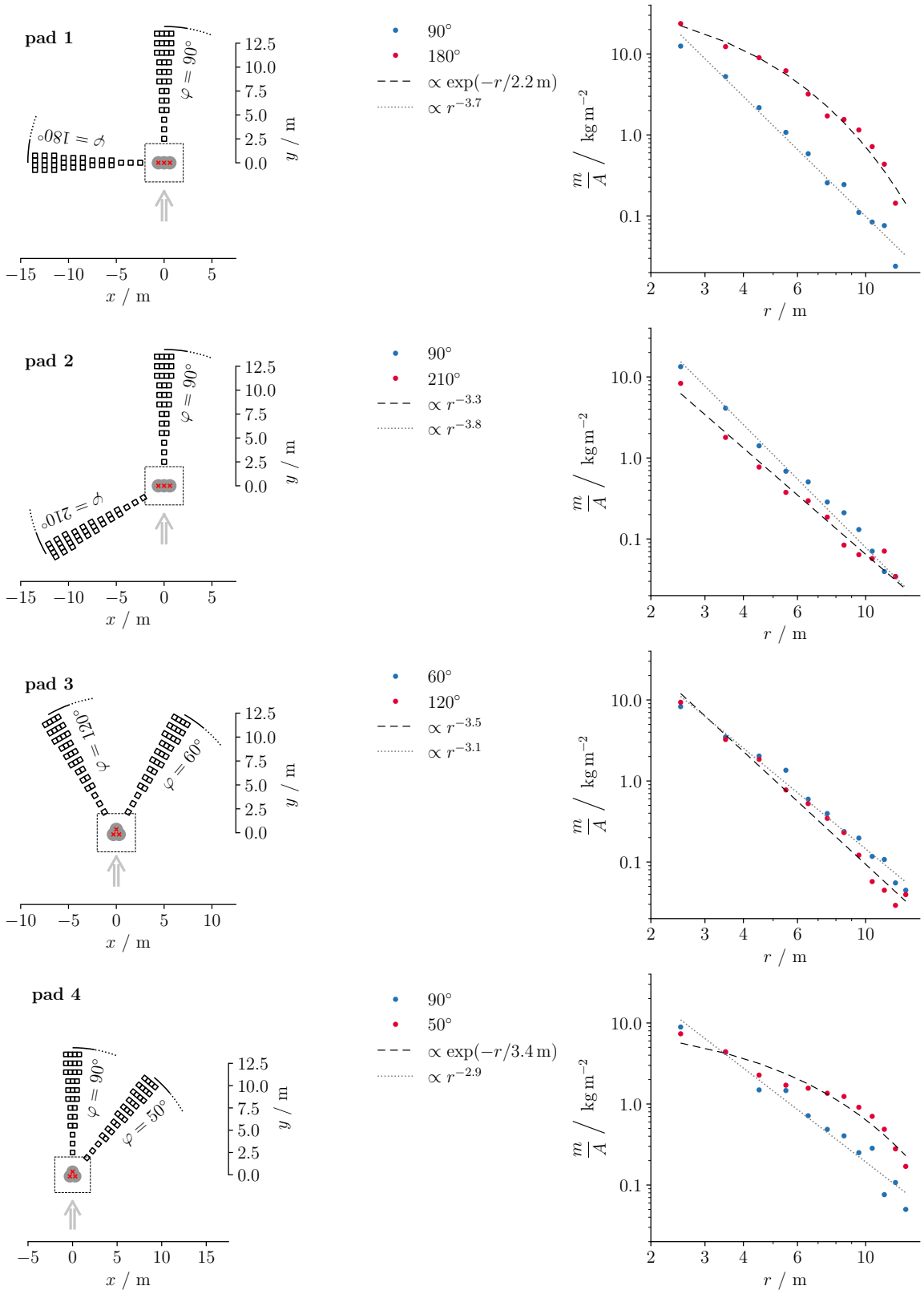

Figure 5: (*Caption on next page*)

Figure 5: Ejecta overview graphs for the four blast sequences ('pads'). ***Left column:*** Map view of layed out ejecta collection box arrays. Each small square represents a $0.5\,\mathrm{m} \times 0.5\,\mathrm{m}$ collection box. At larger distances parallel boxes were used to account for reduced ejecta load. The $2\,\mathrm{m} \times 2\,\mathrm{m}$ square centered at $x, y = 0$ are the test pads, red crosses indicate the charge locations. φ-labels show the polar angle of the collection array. Large gray arrows indicate the main observation direction. ***Right column:*** plots of ejected mass per area at distances r from the crater center. The trends generally follow a power law, except for the 180° case of pad 1 and the 50° of pad 4, for which an exponential trend is a better fit. In those cases larger parts of the material in the main jet direction ended up in the collection boxes. Blue points show that there the decay power of the triangular pads (3 and 4) is slightly less strong than for the linear pads (1 and 2).

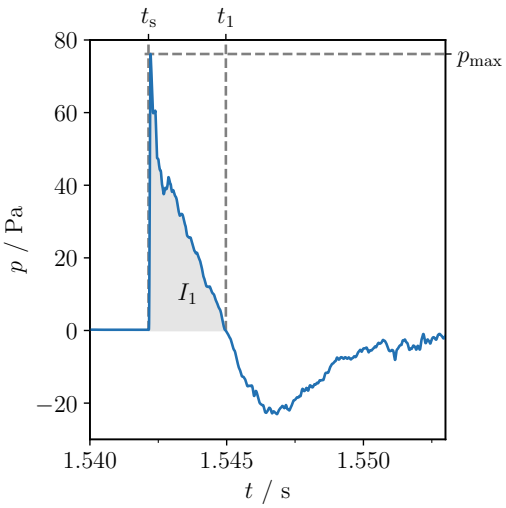

Figure 6: Typical waveform of a blast pulse as recorded by the acoustic microphones; here shown is blast #2 of pad 2, at 82 m distance from source (microphone channel 17). Also shown are characteristic times t_s (shock arrival), t_1 (first zero crossing), maximum pressure p_{max} and impulse of the positive pulse part I_1, that are formulated in Equations 5 and 6.

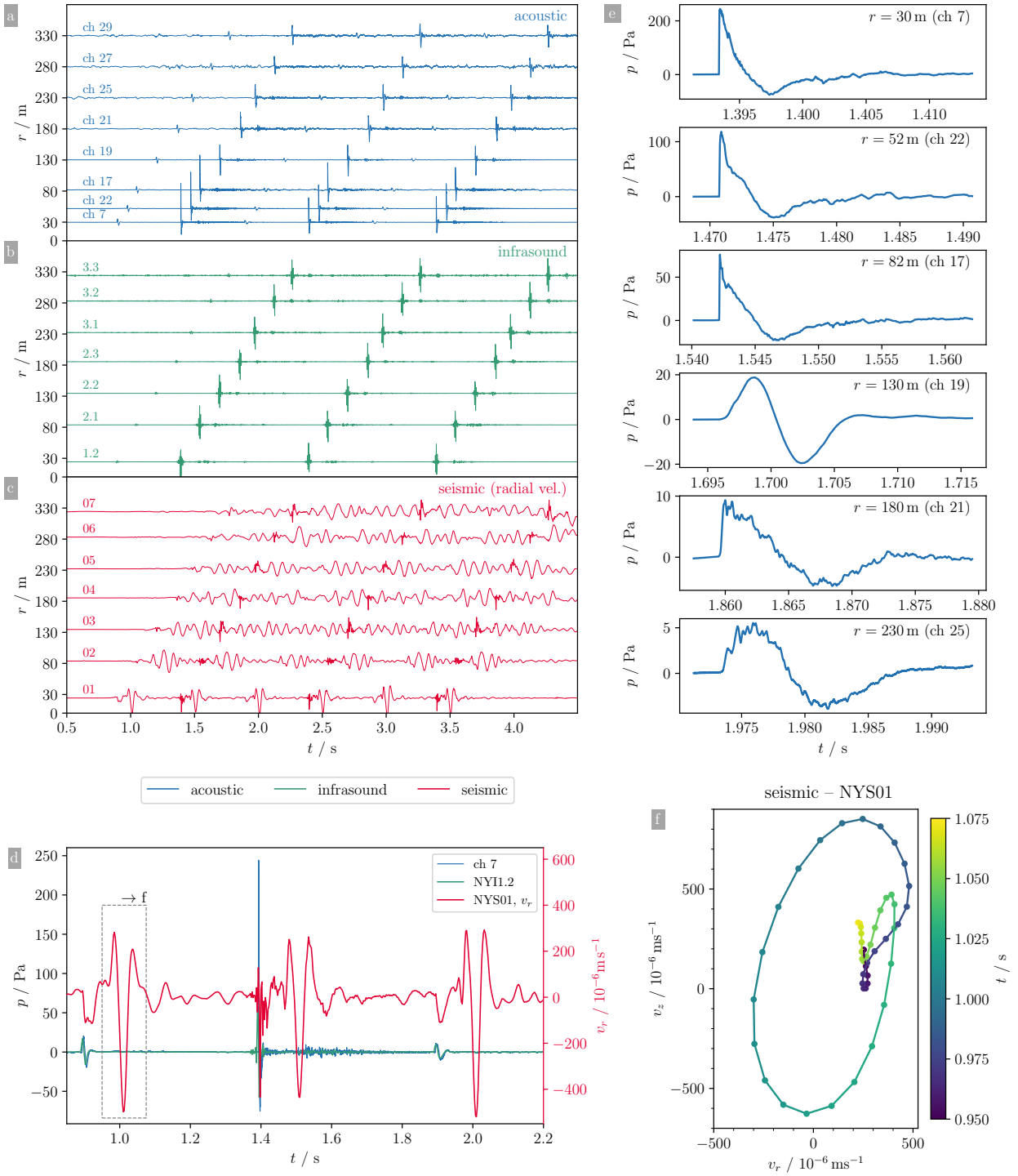

Figure 7: (*Caption on next page.*)

Figure 7: Seismic- infrasound- and acoustic waveform signals of the pad 2 blast sequence. **a, b, c**: The seismic signals show high-frequency coupling at time and location of the large pressure pulses occurrence at the infrasound- and acoustic microphones. **d**: First three pulses at horizontal distance $r = 30\,\mathrm{m}$. High amplitude air-borne pressure waves, such as the acoustic (blue) and infrasound (green) signals at $t \simeq 1.6\,\mathrm{s}$ correlate better with high frequency signal of the seismic channel compared to lower amplitude pulse signals at about 1.1 s and 2.2 s. **e**: Waveforms of microphone records of blast #2 show a clear transition at distance $< 130\,\mathrm{m}$. The 130 m station recorded a more symmetric signal, while at 180 m the rising slope was steeper (asymmetric) again. **f**: Particle motion of the incoming Rayleigh wave created by blast #1. The time window picked for the radial and vertical components is indicated by the dashed rectangle in d.

3.3 Seismo-Acoustics

3.3.1 Radial Dependency of Airborne Blast Pulse

Our recorded pressure pulses show most of the characteristic features of a free air explosion. This indicates that enough energy was not contained in the ground. It is thus possible to estimate the un-contained energy, E_a, which created a shock pulse in the atmosphere. Comparison to the known yield of the detonation charges, E_b, can then give information of the effect of explosion depth.

The more contained blasts did not create large enough blast pulses to make a reasonable comparison with the KG85 reference data. However, all initial and the perceived louder blasts of pads 2 and 4 (blasts 2, 4, 6) created wave forms that were consistent with blast pulses and could be compared. In those cases peak pressure data were in agreement with a $1/r$ dependency at distances of up to 100 m. The impulse data stay consistent up to about 130 m distance (Figure 8a and b). At larger distances the values deviate significantly from $1/r$.

To compare the measured impulse values to the scaled reference, an r^{-1} dependency was fitted to the un-scaled values of a given blast pulse, and the fitting constant a_I was used to determine the location in the scaled graph. This determines an energy, E_a ("atmospheric energy"), that creates the pressure pulse:

$$\begin{aligned} \bar{I}_1 &= \frac{a_{I,\mathrm{ref}}}{\bar{r}} = \frac{a_{I,\mathrm{ref}} E_\mathrm{a}^{1/3}}{f_d r} \\ &= \frac{f_t}{p_\mathrm{a} E_\mathrm{a}^{1/3}} I_1 = \frac{f_t}{p_\mathrm{a} E_\mathrm{a}^{1/3}} \frac{a_I}{r} \end{aligned} \tag{14}$$

$$E_\mathrm{a} = \left(\frac{f_d f_t}{p_\mathrm{a}} \frac{a_I}{a_{I,\mathrm{ref}}} \right)^{3/2} \tag{15}$$

Since both distance and impulse scale with $E_\mathrm{a}^{1/3}$, the procedure 'moves' values on either axis when changing energy (Figure 10). The result are scaled distances at the end of the KG85 reference scale ($\bar{r} \gtrsim 0.6\,\mathrm{m\,J^{-1/3}}$, $100\,\mathrm{m\,kg^{-1/3}}$). From the scaled distance $\bar{r}$ a real distance r corresponds to the energy $E_\mathrm{a} = (f_d r/\bar{r})^3$, which can be interpreted as the energy not contained in the ground, and is smaller compared to the blast energy E_b. E_a was found to be around 1.5% of E_b for the initial

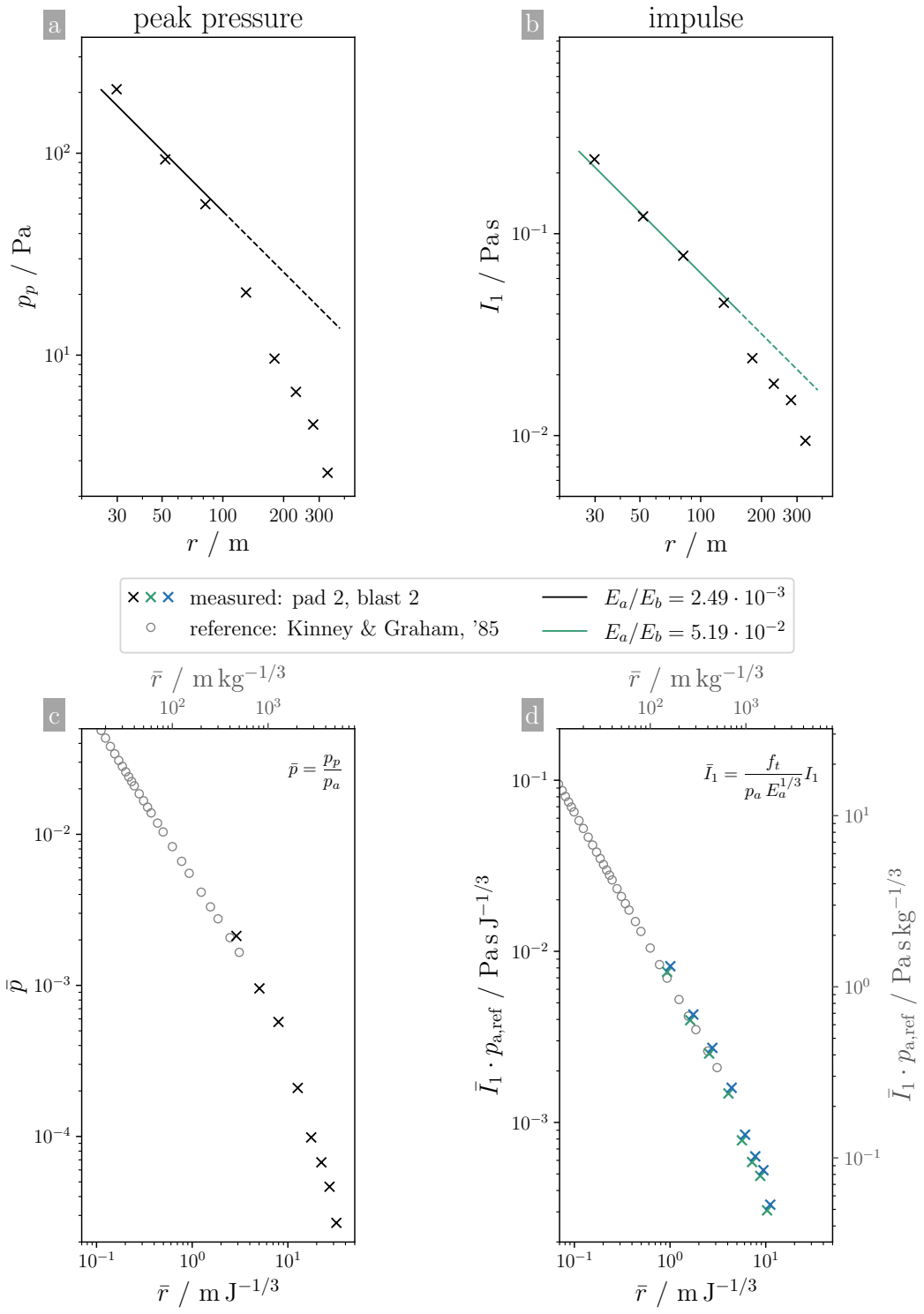

Figure 8: (*Caption on next page.*)

Figure 9: Comparison of peak pressure p_p and impulse I_1 with respect to their applicability to estimate an explosion energy, and their compatibility to the scaled air blast data by Kinney & Graham, 1985 (KG85). **a, b**: Lines show the best fit r^{-1}-dependencies for smaller distances that follow this trend. The impulse data show a better agreement with the r^{-1}-trend. Energies E_a estimated from peak pressures are about a factor 10 smaller compared to the impulse-based estimates. The p_p-values start to deviate significantly from the r^{-1}-trend at distances $r > 100\,\mathrm{m}$. The impulse values start deviating for distances $r > 150\,\mathrm{m}$. **c**: Only the largest blasts produced scaled peak pressures that are comparable to the KG85 values. **d**: Scaled impulse values show a larger overlap with KG85. This is partially caused by the larger energy estimates, which reduce the scaled impulse *and* the scaled radius.

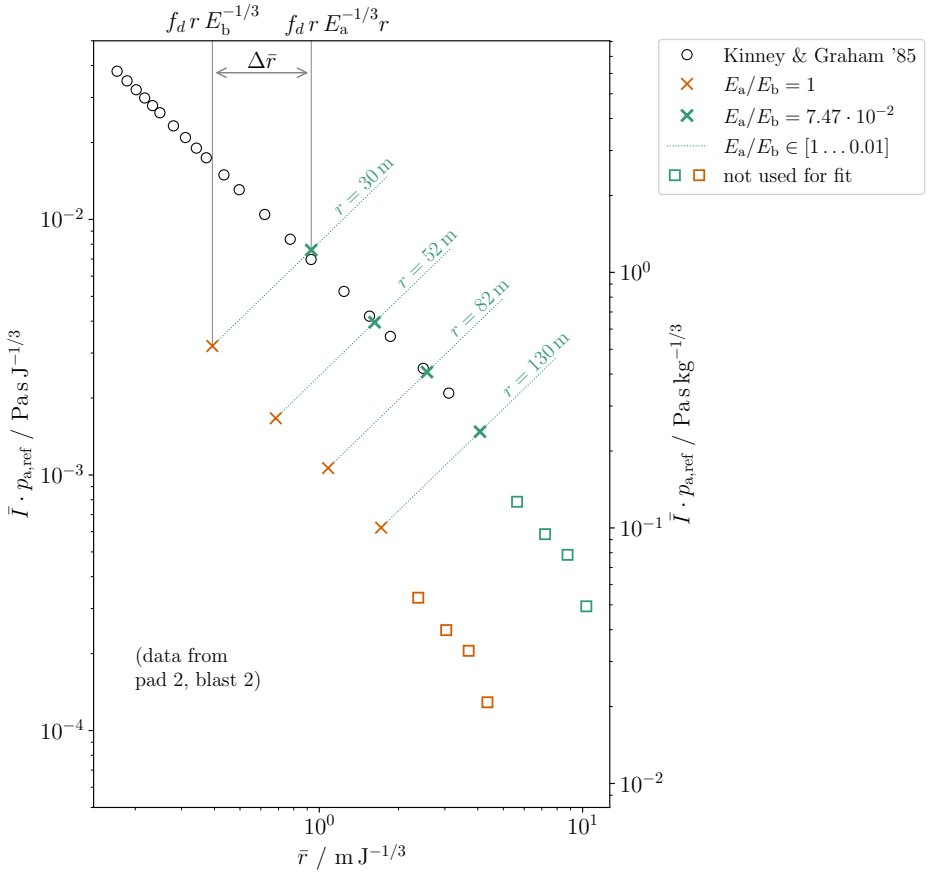

Figure 10: Effect of blast confinement illustrated by a scaled impulse vs. scaled distance plot. Straight forward calculation of scaled distance using the blast's total energy E_b puts the measured scaled impulse (red markers) below the reference values (black circles). The fitting procedure moves the measured values along the green lines. Since both impulse and distance scale with $E^{-1/3}$ their scaled values increase if E decreases. Green markers show values for minimum deviation from reference which correspond to energy E_a.

blasts, and about 5–7.5% of E_b for the perceived loud blasts in pads 2 and 4 (Figure 8c and d, Table 3).

3.3.2 Blast Energy, Charge Depth and Explosion Sequence

The first charge of a blast sequence detonated under a prepared, flat surface in unaltered host material. The following charges detonated under changed topography and somewhat altered host material. The lateral spacing (0.6 m, $8 \times 10^{-3}\,\mathrm{m\,J^{-1/3}}$) corresponds approximately to the maximum crater radius for the blast energy, and similarly, the vertical spacing (0.3 m, $4 \times 10^{-3}\,\mathrm{m\,J^{-1/3}}$) had, approximately, the optimum depth. Previous experiments showed that for such scaled distances the blast's jet changes shape and, if the topography above the charge has an overall orientation, it will also change direction (Ross et al. 2013; Valentine, Graettinger, Macorps, et al. 2015). We follow previous work (e.g. Valentine, White, et al. 2012) and define the explosion depth, d, as the distance from the crater bottom to the charge. With this approximation, i.e. neglecting the crater shape but not its depth, it is possible to evaluate Equation 10 for peak pressures of blasts that were shot at same lateral location for the two different blast delays (0.5 s and 1.5 s) that were realized. For the pad 1 and 3 experiments this applies to the following pairs of blasts: (1, 4), (2, 5), and (3, 6). For the pad 2 and 4 experiments the blast pairs with same lateral location are (1, 2), (3, 4) and (5, 6). Evaluating Equation 10 for two peak pressures at same scaled distance leaves only the scaled depth to change. For example, considering the ratio of peak pressures of pad 2's blasts 2 and 1 relates the scaled depth of blast 2 to the previous one by

$$\bar{d}_{2,\mathrm{r}} = \bar{d}_1 - \bar{d}_0 \,\ln\frac{p_{\mathrm{p},2}}{p_{\mathrm{p},1}} \quad . \tag{16}$$

This formula can be applied to any of the above listed blast couples with consistent results (Figure 11a), showing that the so-derived depths are reduced by a factor 1.5–3, compared to their initial charge location relative to the surface. Since E_b was the same for all blasts, the lower charge at the moment of its detonation can be estimated to be at a depth $d_\mathrm{r} = \bar{d}_\mathrm{r} E_\mathrm{b}^{1/3}$ below the crater bottom at that time. And because the location of the lower charge is known to be 0.6 m below the original surface, the crater bottom can be estimated at $z_\mathrm{bottom} = -0.6\,\mathrm{m} + d_\mathrm{r}$ (Figure 11b). The two delay times show that 0.5 s after detonation the crater bottom is deeper than at 1.5 s. At 1.5 s the crater bottom is about the same location that would be expected from a blast of energy E_b at optimum depth.

Table 3: Results of the acoustic signal analysis: Acoustic energy, E_a, its part of total blast energy, and reduced depths for all experiments. Only signals from the radial microphone line were used. All E_a values were derived from a fit to the impulse-distance relationship (Equations 6 and 8). Only I_1-values that followed an r^{-1}-dependency were used for the fit (Figure 8). For the loud blasts of pads 2 and 4 (blasts 2, 4, 6) the r^{-1} dependency ended for $r > 130\,\mathrm{m}$. which was the case for microphones at distances up to 130 m ($\bar{r} \leq 1.71\,\mathrm{m\,J^{-1/3}}$, $276\,\mathrm{m\,kg^{-1/3}}$).

Pad	Blast	mics used[1]	Distance range[2] (m)	E_a $\times 10^3$ J	$E_\mathrm{a}/E_\mathrm{b}$ %	d_red	$\bar{d}_\mathrm{red}$ $\times 10^{-3}\,\mathrm{m\,J^{-1/3}}$
1	1	6	31.2–280	4.32 ± 0.52	0.99 ± 0.12	0.30	3.95
	3	6	31.2–280	3.88 ± 0.51	0.89 ± 0.12	0.30	3.95
	2	6	31.2–280	4.48 ± 0.80	1.03 ± 0.18	0.30	3.95
	4	4	31.2–280	1.71 ± 0.11	0.39 ± 0.02	0.36	4.72
	5	3	31.2–280	2.59 ± 0.25	0.59 ± 0.06	0.32	4.21
	6	3	31.2–280	1.11 ± 0.06	0.25 ± 0.01	0.35	4.62
2	1	8	29.8–330	7.92 ± 0.49	1.81 ± 0.11	0.30	3.95
	2	4	29.8–130	32.62 ± 1.61	7.47 ± 0.37	0.20	2.67
	3	–	–	–	–	0.30	3.95
	4	4	29.8–130	33.37 ± 0.67	7.64 ± 0.15	0.17	2.30
	5	7	29.8–330	3.62 ± 0.44	0.83 ± 0.10	0.30	3.95
	6	4	29.8–130	28.92 ± 1.62	6.62 ± 0.37	0.19	2.44
3	1	6	28.1–280	6.17 ± 1.39	1.41 ± 0.32	0.30	3.95
	2	6	28.1–280	6.28 ± 0.91	1.44 ± 0.21	0.30	3.95
	3	6	28.1–280	16.10 ± 1.83	3.69 ± 0.42	0.30	3.95
	4	3	28.1–80.7	3.13 ± 0.24	0.72 ± 0.06	0.33	4.33
	5	5	28.1–280	6.79 ± 0.68	1.56 ± 0.16	0.30	4.00
	6	3	28.1–80.7	4.41 ± 0.30	1.01 ± 0.18	0.07	5.05
4	1	4	48.6–180	5.82 ± 0.61	1.33 ± 0.14	0.30	3.95
	2	3	48.6–130	23.63 ± 0.79	5.41 ± 0.18	0.22	2.91
	3	4	48.6–180	3.66 ± 0.37	0.84 ± 0.08	0.30	3.95
	4	3	48.6–130	25.21 ± 0.96	5.78 ± 0.22	0.22	2.93
	5	4	48.6–180	6.39 ± 0.31	1.46 ± 0.07	0.30	3.95
	6	3	48.6–130	28.80 ± 1.10	6.60 ± 0.25	0.24	3.22

[1]: Number of microphones used to fit the radial dependency to the data.
[2]: Minimum and maximum distance of the microphones used to determine E_a.

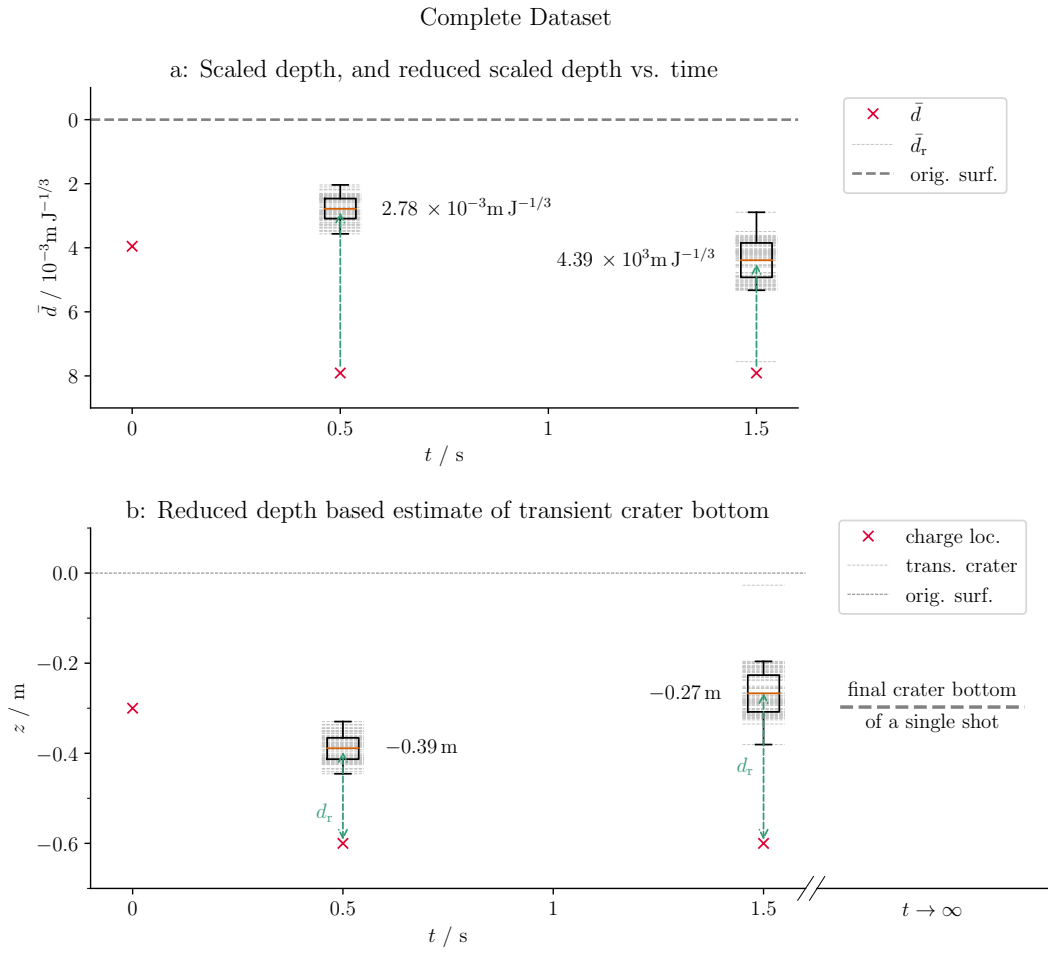

Figure 11: Scaled charge depths (red crosses), reduced scaled depths (gray, dashed lines: values of a single microphone, orange: average of all microphones) of all microphone sensors at one angle, plotted against time after detonation of the previous charge located vertically above. a: At 0.5 s delay, scaled depth is reduced by a factor 2–3 compared to original charge location. At 1.5 s delay scaled depth is only reduced by a factor 1.5–2. (b) Estimated of the time dependent crater bottom evolution. For comparison the dashed gray line shows the measured depth of a single shot of same charge type and energy.

Pad	Measured Footprint		Reduced Footprint		Max. Footprint	
	Area m^2	Radius m	Area m^2	Radius m	Area m^2	Radius m
1	3.71	0.78	3.97	0.81	4.26	0.85
2	3.38	0.73	3.73	0.78	4.26	0.85
3	2.79	0.68	3.76	0.83	3.92	0.85
4	3.13	0.73	3.71	0.82	3.92	0.85

Table 4: Measured-, reduced- and maximum-expected crater sizes for the tested explosion configurations. The reduced footprint is the maximum possible footprint when blasting at the reduced depth. The maximum footprint is the overall maximum that can be expected from the given blast energy.

3.3.3 Seismic Signal

We present here an initial estimate of seismic energy involved in the explosion experiments. A deep analysis of the seismic records will be part of future studies. The energy radiated from a radially symmetric seismic source may be estimated from the measured square velocity of the ground (particle) motion u_r (e.g. Boatwright 1980; Johnson et al. 2005)

$$E_\mathrm{s} = 2\pi r^2 \frac{\rho_\mathrm{g} c_\mathrm{g}}{A} \int_0^\infty S\, u_r^2(r,t)\; dt \quad . \tag{17}$$

Here A and S are coefficients for signal attenuation and site response, respectively. ρ_g is the ground density and c_g the propagation speed of the ground, both at the observation location. For this first broad look at seismic energy these parameters are assumed to be constant. In this assumed energy estimate only one component of ground motion, radial component u_r is non-zero. Other seismic components are therefore ignored in the following. Then E_s can be approximated as

$$E_\mathrm{s} \simeq F\, r^2 \int_0^\infty u_r^2(r,t)\, dt \quad , \quad F = 2\pi \rho_\mathrm{g} c_\mathrm{g} \frac{S}{A} \quad . \tag{18}$$

In this approximation the proportionality factor F depends on a combination of ground properties and attenuation characteristics, but not on E_s.

The multi-blast setting adds the difficulty that seismic signals originating from different blasts overlap at larger distances (e.g. for $r \gtrsim 80\,\mathrm{m}$, Figure 7c). From such distances only the cumulative seismic energy of a blast set can be determined:

$$\sum_{i=0}^{N_\mathrm{b}} E_{\mathrm{s},i} = F\, r^2 \int_0^\infty u_r^2(r,t)\, dt \qquad (\text{here } N_\mathrm{b} = 6). \tag{19}$$

At closer ranges the blasts can be identified clearly in the u^2 signal. There u^2 decays quickly before

the next pulse arrives, and integration over a finite time interval is a valid approximation for each blast (Figure 12a):

$$E_{\mathrm{s},i} = F\, r^2 \int\limits_{\Delta t_i} u_r^2(r,t)\, dt \tag{20}$$

When compared to the airborne signals, the seismic records show an inverted trend: The "muffled" blasts 1, 3 and 5 of pads 2 and 4, which had a much lower airborne signal created a larger seismic signal, when compared to blasts 2, 4 and 6 (Figure 12a). This behavior serves as motivation for a potential energy partitioning scheme. For a given pad configuration the assumption is made that seismic and acoustic energy of a blast add up to a constant value.

$$E_{\mathrm{b}} = E_{\mathrm{a}} + E_{\mathrm{s}} + E_{\mathrm{rem}} \tag{21}$$

In this picture a change in E_{a} of δE, for example by a change of blast depth, would result in a change of E_{s} by $-\delta E$. The remaining energy E_{rem} stays constant. E_{rem} may be viewed as a term that gathers the energy of all other parts of processes involved, including dissipation such as heat, friction and brittle deformation. The assumption that it is a constant means that changing the airborne energy, for example by changing the blast's containment (depth), only changes seismic energy. The two 'generalized elastic' terms can exchange energy, while the remainder term does not.

Energy conservation applies to each blast and to the cumulative case, which allow determination of the two unknowns F and E_{rem}. With $\Delta E = E_{\mathrm{b}} - E_{\mathrm{rem}}$ the per-blast case becomes

$$r^2 \int\limits_{\Delta t_i} u_r^2(r,t)\, dt = \frac{E_{\mathrm{s},i}}{F} = \frac{\Delta E - E_{\mathrm{a},i}}{F} \quad , \tag{22}$$

and the cumulative case is

$$\begin{aligned} \int\limits_0^\infty u_r^2(r,t)\, dt &= \frac{N_{\mathrm{b}} E_{\mathrm{b}} - N_{\mathrm{b}} E_{\mathrm{rem}} - \sum E_{\mathrm{a},i}}{F\, r^2} \\ &= N_{\mathrm{b}} \frac{\Delta E - \langle E_{\mathrm{a}} \rangle}{F\, r^2} \quad , \end{aligned} \tag{23}$$

where $\langle E_{\mathrm{a}} \rangle = \sum E_{\mathrm{a},i} / N_{\mathrm{b}}$. The difference between the two cases is that for Equation 23 r is treated as independent variable, while in Equation 22 E_{a} is independent. The average value $\langle E_{\mathrm{a}} \rangle$ is a constant.

The left hand side values of Equation 23 were fitted to an r^{-2} dependency. The result shows the expected behavior: Pads 2 and 4 with the large airborne signals have smaller seismic signals when compared to their respective geometric counterparts pads 1 and 3 (Figure 12b). The per-blast data for the right-hand side of Equation 22 show a different trend of the pad 3 data compared to the other pads (Figure 12c). For small E_{a} they are larger than the other pads, and then fall off quicker with rising E_{a}. Since for the other pads no unique trend could be determined, pad 3 was treated separately, from pads 1, 2 and 4. For both cases intercept and slope were determined. Together with the cumulative case fit, values for ΔE and F were calculated. For pads 1, 2 and 4, ΔE was

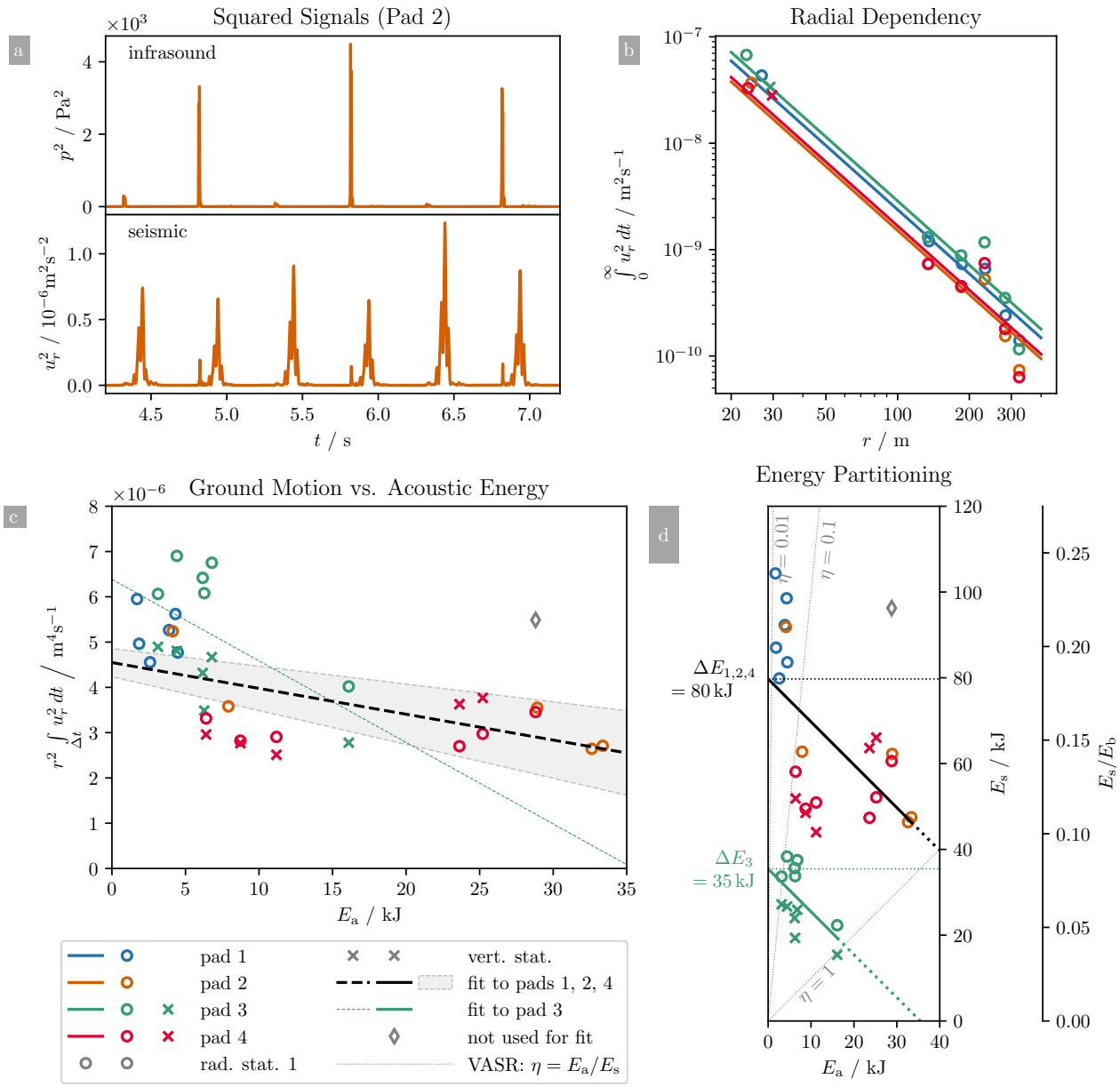

Figure 12: Estimate of seismic energy from squared particle velocity. **a:** Pad 2 test squared pressure signal of the infrasound sensor and squared particle velocity at first radial station (30 m distance). The seismic signal shows clearly identifiable pulses that can be separated into six time intervals. As described earlier for pad 2 the airborne pressure pulses of blasts 1, 3 and 5 are much weaker as those of blasts 2, 4 and 6. In contrast peak values of u_r^2 are higher for blasts 1, 3 and 5, and somewhat weaker for blasts 2, 4 and 6. The trend is not as strong for the seismic signal as it is for the airborne signal. **b:** Radial dependency of squared particle velocity integral. Measured values and fitted r^{-2} curves of Equation 23 are shown. Pads 1 and 3, with sequential shot depth configuration, produced a higher squared particle velocity integral, compared to pads 2 and 4 (interchanging blast depth). To a lesser degree, the triangular pads 3, and 4 had larger values when compared to the same shot depth configuration of the linear geometrical setups of pads 1, and 2. (*Caption continues...*)

Figure 12: (*... Continued*) **c:** Squared particle velocity integral dependency on E_a. Despite some scatter, data from pads 1, 2 and 4 follow a common trend, while pad 3 data has a larger slope and offset. The black dashed line is a fit of Equation 22 to data of pads 1, 2, and 4 (correlation coeficient 0.67). The green dotted line to the pad 3 data (correlation coeficient 0.69). Cross markers show data form type A station closest to the blasts, circles data from the type B station. **d:** Seismic energy plotted against acoustic energy for all pads. Black and green lines show the anticipated (linear) relationships using the derived values for F and ΔE. The second vertical axis shows E_s relative to total blast energy E_b. The elastic part is ca. 17% of E_b for pads 1, 2, 4 and ca. 10% for pad 3. Gray dotted lines show the volcanic acoustic seismic ratio $\eta = E_a/E_s$ (VASR, Johnson & Aster, 2005). The blasts had VASR values between 10^{-2} and 1.

---

about 17% of E_b ($\simeq 73\,\mathrm{kJ}$), for pad 3 this value is about 10% ($\simeq 45\,\mathrm{kJ}$). Highest values of E_s are a factor two larger than highest values of E_a. Consequentially in cases of observed higher E_a blasts, seismic and airborne energies were comparable (Figure 12d). To be complete, values for F are $3.5 \times 10^9\,\mathrm{Js\,m^{-4}}$ for pads 1, 2, 4, and $1.6 \times 10^9\,\mathrm{Js\,m^{-4}}$ for pad 3.

4 Discussion

The sizes of the presented craters are larger than one-blast craters, but smaller than they could become when blasting many times (i.e. $n \gtrsim 4$) at these lateral locations with the same energy. Overlapping footprints from laterally shifting, time-separated explosions create compound craters with a footprint area that can be calculated from overlapping circles centered around blast locations (Valentine, Graettinger, Macorps, et al. 2015). For a given explosion depth a radius is related to explosion energy by the scaled radius, and therefore the footprint area is, too. Evaluating Equation 13 for $n = 1$ relates the scaled crater radius after one blast r_1 to the scaled upper limit for many blasts $\bar{r}_\infty$. Solving for $\bar{r}_\infty$ and multiplying by $E_b^{1/3}$ yields the upper limit for this blast energy

$$r_{\infty,\max} = \frac{r_{1,\max}}{1 - e^{-1/n_0}} \simeq 1.49\ \bar{r}_{1,\max}\, E_b^{1/3} = 0.85\,\mathrm{m} \quad . \tag{24}$$

Here $\bar{r}_{1,\max} = 7.5 \times 10^{-3}\,\mathrm{m\,J^{-1/3}}$ is the maximum scaled radius of one explosion, which occurs at the optimum scaled depth and was measured in previous experiments (Sonder, Graettinger, and Valentine 2015). For repeated blasting at reduced depths an equivalent crater size, $r_{\infty,\mathrm{red}}$ can be calculated by replacing $r_{1,\max}$ in Equation 24 with $r_{1,\mathrm{red}}$. The measured footprint radii fit into this picture: they range between 0.68 m and 0.78 m, which is larger than the single explosion radius ($r_{1,\max} = \bar{r}_{1,\max} E_b^{1/3} = 0.57\,\mathrm{m}$) and smaller than the many-blasts limit. However, the crater sizes are not consistent with respect to the blasting sequence: in case of the linear setup, pad 1 (upper before lower charges) created a larger crater compared to pad 2 (interchanging charge depths), while in the case of the triangular setup pad 4 (interchanging depths) created the larger crater when compared to pad 3 (Table 4).

Equation 24 can also be used to estimate the final crater size of a hypothetical crater that would be the result of many blasts at reduced depth. It is then necessary to replace the maximum (scaled)

crater radius with the reduced radius. The latter can be calculated from the scaled radius- scaled depth dependency for a single blast ($\bar{r}_1(\bar{d}_\mathrm{r})$, Equation 11), using the scaled reduced depth value:

$$\bar{r}_{\infty,\mathrm{r}} = \frac{\bar{r}_\mathrm{r}}{1 - e^{-1/n_0}} \simeq 1.49\ \bar{r}_1(\bar{d}_\mathrm{r}) \tag{25}$$

A footprint size estimated this way is larger than the measured two-blast crater, and ca. 7% smaller compared to the maximum possible crater (Table 4, Figure 13).

Goto, Taniguchi, et al. (2001) report that they conducted repeated blast experiments at same lateral location, and observed that the crater size only changed if the blast energy increased compared to the initial blast. This is an apparent difference to the results presented here and by Graettinger, Valentine, Sonder, Ross, White, and Taddeucci (e.g. 2014), Ross et al. (2013), Sonder, Graettinger, and Valentine (2015), and Valentine, White, et al. (2012) who report scaled sizes of multi-blast craters that are larger than that of a single blast. Goto, Taniguchi, et al. (2001) do not provide information on the explosion location, i.e. whether the following charge was placed at same depth below the original surface, or at same depth under the crater bottom, or at some other depth. Therefore it may be permissible to speculate that the charges were placed at same absolute position (same distance to original surface) as the initial charge, which would correspond to an explosion depth reduced by the crater depth. Their reported data suggest that in this case the scaled depth would be lower than the optimal scaled depth that creates the largest crater, and therefore the repeated blasts could not increase the crater size.

Determination of the atmospheric energy E_a from airborne impulse or peak pressure is possible for scaled distances up to about $5\,\mathrm{m\,J^{-1/3}}$ ($800\,\mathrm{m\,kg^{-1/3}}$). At larger distances this type of analysis yields faulty values. A word of caution must be added, since the empirical models by Kinney et al. (1985) and Ford et al. (2014) yield a factor 2 to 3 different energy estimates. A more in-depth analysis that focuses on the complete seismo-acoustic dataset of the presented experiments may help here. For example, peak pressure of a weak shock (e.g. Muhlestein et al. 2012; Rogers 1977; Young et al. 2015) decays with a power of radius slightly larger than 1. Such a dependency may be observed in the presented data (Figure 8a). Other non-linear acoustic factors and near-field topography may also play a role (Maher et al. 2020). Nevertheless, both models evaluated here result in single digit values for the percentage of the energy ratio $E_\mathrm{a}/E_\mathrm{b}$. The relatively small amounts of explosives used have the advantage that the analysis does not have to deal with complications arising from drastically changing transmission factors (Equation 4), as in the case of large scale explosive events (e.g. Kim et al. 2016; Kim et al. 2017) or volcanic eruptions (Matoza, Garcés, et al. 2009).

For application to volcanic scale this validity range means that sensors would need to be deployed at a maximum range which depends on the explosion's energy and depth. Phreatomagmatic eruptions typically produce explosions with energies in a range of $10^9\,\mathrm{J}$ to $10^{13}\,\mathrm{J}$ (240 kg TNT to 2.4 kt TNT, respectively) (Valentine, Graettinger, and Sonder 2014). An explosion that occurs at a scaled depth of $4 \times 10^{-3}\,\mathrm{m\,J^{-1/3}}$, which creates the largest craters at a given energy and corresponds to non-scaled depths 2 m and 86 m for above energy range, respectively. According to our results, at that depth about 1% of the energy would go into the airborne pulse, which corresponds to a maximum range of about 1 to 23 km, assuming $5\,\mathrm{m\,J^{-1/3}}$ as maximum applicable scaled range

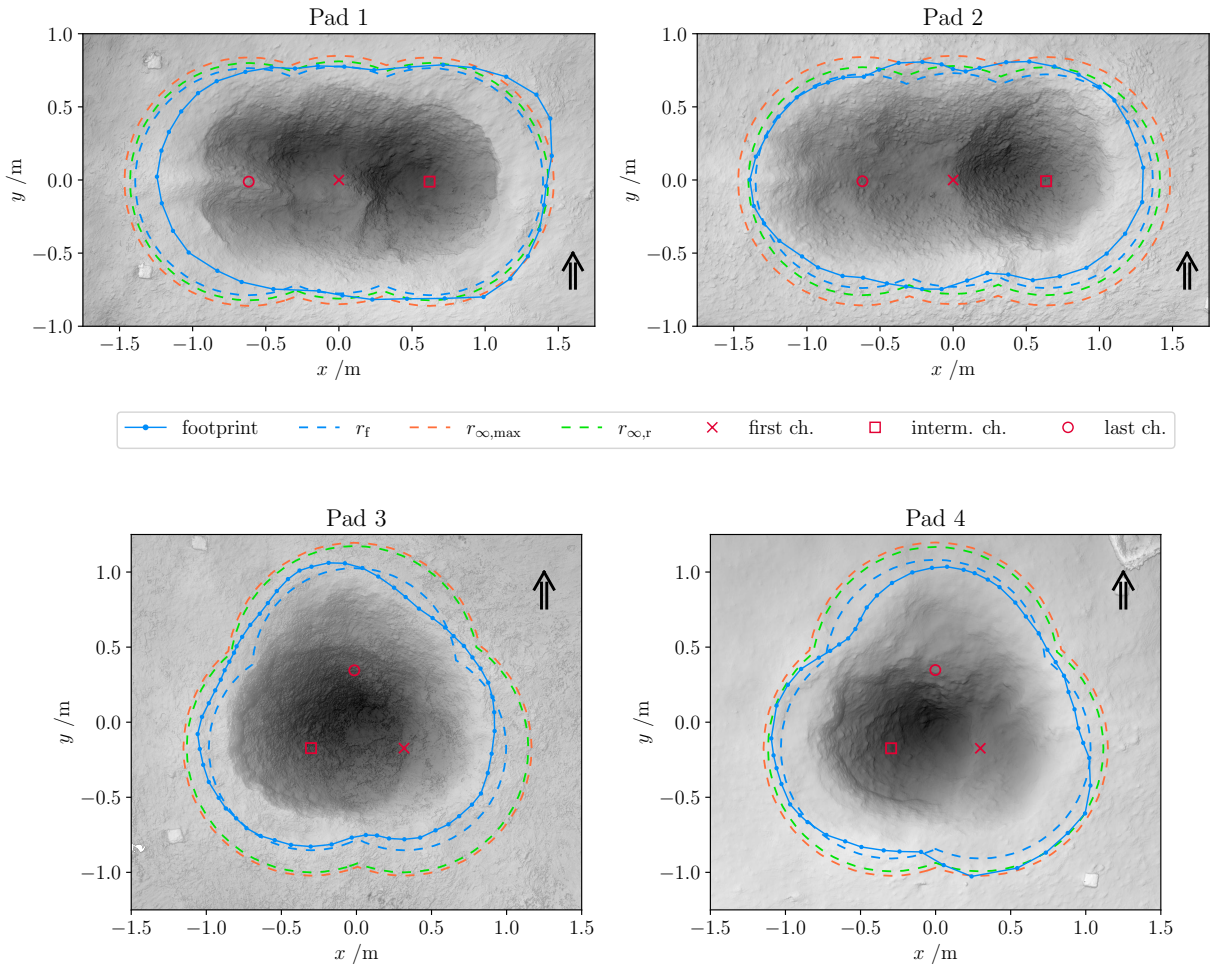

Figure 13: Map views of the four craters, their footprints, and footprint equivalent circles of corresponding radii. Red markers in the footprint show locations of first, intermediate and last charge, respectively. Main observation direction was towards positive y (black arrows). All radii correspond to an explosion energy, $E_b = 4.635 \times 10^5$ J. Blue lines represent the measured footprint (topographic high). Blue dashed circles are the radii matching the footprint's area. Red lines represent the maximum possible footprint ($r_{\infty,max}$) that can be expected from this blast energy. Green lines show the hypothetical footprint ($r_{\infty,r}$) that would be the result of many (> 3) explosions at the average reduced depth as measured in each pad.

(Figure 8). For smaller events, sensors would have to be placed closer to a vent.

The changes in the apparent ("reduced") crater depth over time show that 0.5 s after detonation the crater is about a factor 1.5 deeper compared to 1.5 s after detonation. It is not clear whether this is the time of the transient cavity's maximum opening or not. The depth at 1.5 s is comparable to the depth of a single blast crater. For volcanic activity the timescale on which a crater forms is important. In this period part of the overlying mass confining magma in the ground is rapidly reduced, changing- or enabling non-steady state processes, such as magma-water mixing and phreatomagmatism (Büttner et al. 1998; Lorenz 1975) or decompression driven activity (Gonnermann et al. 2007). Assuming for a moment that crater formation duration scales with $E_{\mathrm{b}}^{1/3}$, analogous to other blast related time and length (e.g. blast depth, crater radius), the presented results mean that for $E_{\mathrm{b}} = 0.4365\,\mathrm{MJ}$ crater formation lasts on the order of 1 s, which corresponds to a scaled duration of $1.3 \times 10^{-2}\,\mathrm{s\,J^{-1/3}}$. An event creating a crater of about 15 m diameter would need 10^9 J (Valentine, Graettinger, and Sonder 2014) if created by a single blast, and would be formed in $1.3 \times 10^{-2}\,\mathrm{s\,J^{-1/3}} \times 10^3\,\mathrm{J^{1/3}} = 13\,\mathrm{s}$. A 25 m diameter crater would then need 44 s to form. It is, however, likely that other factors, such as variations in the host's material strength, complicate such a straight forward scaling approach. We note that previous work by Ohba et al. (2002) reported cube-root scaled 'explosion cloud duration' dependency of scaled explosion depth of the same order. At optimum depth this scaled duration is $4 \times 10^{-3}\,\mathrm{sJ^{-1/3}}$, corresponding to ca. 0.3 s.

Despite such scaling difficulties the experiments show that hazards associated with explosions in the subsurface should be reevaluated. Multiple blasts may produce craters that allow deeper explosions to release energy at the surface, once they are no longer contained by excess load. Valentine, Graettinger, and Sonder (2014) found that for well time-separated blasts, explosions at scaled depths equal or deeper than $8 \times 10^{-3}\,\mathrm{m\,J^{-1/3}}$ do not erupt at the surface, but form subsidence pits, and have therefore a reduced hazard potential. The lower charges in this study were located 0.6 m below the original surface, which corresponds to a scaled depth of $8 \times 10^{-3}\,\mathrm{m\,J^{-1/3}}$, and would therefore stay contained in a single shot. The deeper lying charges of the pad 2 and 4 blast sequences not only erupted, but released significantly more energy into the atmosphere than the shallower charges, because explosion timing was such that the crater cavity was open. This effect corresponds to an effective reduction of scaled explosion depth by 65 % 0.5 s after the upper charge and by 45 % 1.5 s after the upper charge (Figure 11a). We note that such scaled depth reductions are equivalent to 22× and 5× increase in explosion energy (at same depth), respectively. The scenario of successively crater deepening, which is also of military interest (Antoun et al. 2003), cannot repeat indefinitely, since the following crater needs to move material from greater depth to the surface in a finite time window, which needs energy. More experiments are necessary to test where this limit lies, and what the exact crater formation duration is.

Analysis of the seismic signal reveals why the pad 3 crater is smaller compared to pad 4: Pad 3 had different attenuation- and coupling conditions leading to less energy available for seismic and acoustic pressure or momentum generation (ΔE), and more energy dissipated without momentum generation. The different coupling is the result of a variation in the pads host properties: On a subjective level, personnel preparing the pad for charge placement before blasting can confirm that

pad 3 'felt' somewhat different compared to the others when punching holes for charge placement into the material. Such unintentional host variability highlights the sensitivity of the crater formation process to host properties (see also Macorps et al. 2016). The estimate of seismic energy and the energy partitioning analysis rely on good knowledge of E_a. The assumptions made to estimate E_s work well for large values of E_a. At smaller E_a (more contained blasts) scatter becomes larger, which suggests that the underlying assumption, that energy is partitioned only between seismic and airborne signal producing effects, does not apply there. The squared velocity and pressure signals of pads 1 and 3 emphasize this trend (Supporting Information Figure S9 and Figure 12a). In a first order estimate the combined data from blasts in pads 1, 2 and 4 was between 10% and 20% of E_b, and between 5% and 10% of E_b for the blasts of pad 3. The experiments show how explosive energy is contained by friction, strength and inertia of the surrounding (overlying) material and how energy translates from driving ground-bound (seismic) to airborne processes, once the overarching containment parameter, scaled depth $\bar{d}$, is reduced.

Changes in host density and strength can make it harder to observe above phenomena on natural scale. Attenuation and site-specific response (Equation 17) depend on the host's strength and density, both of which also depend on the moisture content of the ground (e.g. Lamb et al. 1991; Rickman et al. 2011). Part of the energy which does not cause seismic or airborne waves is likely used to fragment the host rock (Dürig, Ross, et al. 2021; Ouchterlony et al. 2019). Even though fragmentation is an important part of explosive volcanic processes (Zimanowski, Wohletz, et al. 2003), the size of the presented experiments did not allow one to measure changes in collected representative samples of the ejected material. One-shot experiments in hard rock hosts show a strong decay of crater radius at scaled depths larger than 'optimum' excavation depth (Rocco et al. 2010). If a blast sequence occurs in a hard rock environment the first blast likely fragments more material than following blasts (assuming similar energies), and consequently less energy would be available for other types of dissipation and elastic processes. Our experiments show that even in unconsolidated material large parts of a blast's energy is dissipated by fragmentation or friction.

5 Conclusions

Rapidly-timed subsurface blasts, occur in fields such as mining, geotechnical, military and medical applications (Arora et al. 2017; Mammadova et al. 2017; Qiu et al. 2018; Zhou et al. 2016). Our analysis of the ejecta, crater morphology, and seismo-acoustic signals should be applicable to those situations. We highlight volcanic eruptions, which commonly involve explosions in rapid succession (Dürig, M. T. Gudmundsson, et al. 2015; Pistolesi et al. 2011). The results of this study provide insight on how to quantitatively interpret geophysical signals measured during such eruptions, as well as the resulting craters and deposits. The experiments show that energy is a robust parameter to relate the transient, dynamic phenomena, such as airborne and seismic pressure and stress waves and debris jets, with the long term products such as crater, subsurface deposits and ejecta. The observed changes of crater size due to the different charge sequence arrangements are on the same order as changes expected from different rock strength or water content (Nordyke 1961;

Rickman et al. 2011). Explosions from depths which, in well time separated settings, would stay contained in the ground, may breach the surface and erupt. They may breach if containment is temporarily reduced by a previous blast at smaller depth. The depth reductions observed in the presented experiments correspond to an energy increase up to a factor of 22. We emphasize that much of the presented physical signal analysis relies on (a) the high frequency records of airborne signal and (b) on the combination of relative near-field and far-field records. Deployment of such sensors hold promise for progress in seismo-acoustic volcano monitoring. Finally, the combined analysis of crater size and airborne signal showed the time dependency of the transient crater cavity. For the 0.44 MJ blast energy used here the transient crater is deeper 0.5 s after the blast than at 1.5 s. We think that this is important for the analysis of explosive volcanic blast dynamics.

Appendix

A Depth- and Distance Dependency of Peak Pressures from Previous Experiments

In previous blasting experiments (Graettinger, Valentine, Sonder, Ross, White, and Taddeucci 2014; Ross et al. 2013; Sonder, Graettinger, and Valentine 2015; Valentine, Graettinger, Macorps, et al. 2015), a set of uncalibrated microphones was placed every 5 m starting at 5 m to 30 m distance from the source. In all experiments the microphones were placed 10 cm above the ground facing towards the blast center. The blasts happened at various scaled depths with an emphasis roughly around optimum excavation conditions ($\bar{d} \simeq 4 \times 10^{-3}\,\mathrm{m\,J^{-1/3}}$), but also deeper and some shallower blasts. Despite the uncalibrated pressure signal the raw signals were evaluated, since all sensors were of same model and therefore comparable. The result can be used to determine the relative depth dependency of impulse- and pressure signals, and compare them to other work (e.g. Ford et al. 2014). Signals were evaluated for peak pressure and impulse the same way as described for the here presented experiments in the main text.

Results show that the expected exponential depth dependency (Equation 9) underestimates both, pressure and impulse for deeper blasts (Figure 14). Therefore a second term that only depends on scaled distance was added to the combined depth- and distance dependencies

$$p_{\mathrm{p}}(\bar{d},\bar{r}) = \frac{C_{\mathrm{p,1}}}{\bar{r}}\, e^{-\bar{d}/\bar{d}_{p,0}} + \frac{C_{\mathrm{p,2}}}{\bar{r}} \quad , \tag{26}$$

$$\bar{I}(\bar{d},\bar{r}) = \frac{C_{\mathrm{i,1}}}{\bar{r}}\, e^{-\bar{d}/\bar{d}_{i,0}} + \frac{C_{\mathrm{i,2}}}{\bar{r}} \quad . \tag{27}$$

At scaled depths smaller than $1.2\,\bar{d}_{\mathrm{opt}}$ ($\simeq 5 \times 10^{-3}\,\mathrm{m\,J^{-1/3}}$) the first term dominates, and the peak pressure show an exponential dependency (Figure A1). At larger scaled depths peak pressures decay slower than this exponential predicts. More research is necessary, to clarify the slow decay. Bowman et al. (2014) suggest that ground motion dominates the airborne signal at larger depths. Best fitting values for the depth decay constant in the exponential is for the pressure case $\bar{d}_{p,0} = (5.4 \pm 0.5) \times 10^{-4}\,\mathrm{m\,J^{-1/3}}$, and for the impulse case $\bar{d}_{i,0} = (1.1 \pm 0.3) \times 10^{-3}\,\mathrm{m\,J^{-1/3}}$. $\bar{d}_{i,0}$ deviates by about 12% from the value found by Ford et al. (2014) responsible for depth decay ($\bar{d}_3$, Table 6). We interpret this as good agreement for the range $0 \leq \bar{d} \leq 5 \times 10^{-3}\,\mathrm{m\,J^{-1/3}}$.

B Interpolation Constants of KG85 Pressure and Impulse

The empirical equations for dependencies of blast overpressure, scaled impulse and scaled blast duration on scaled distance are as follows.

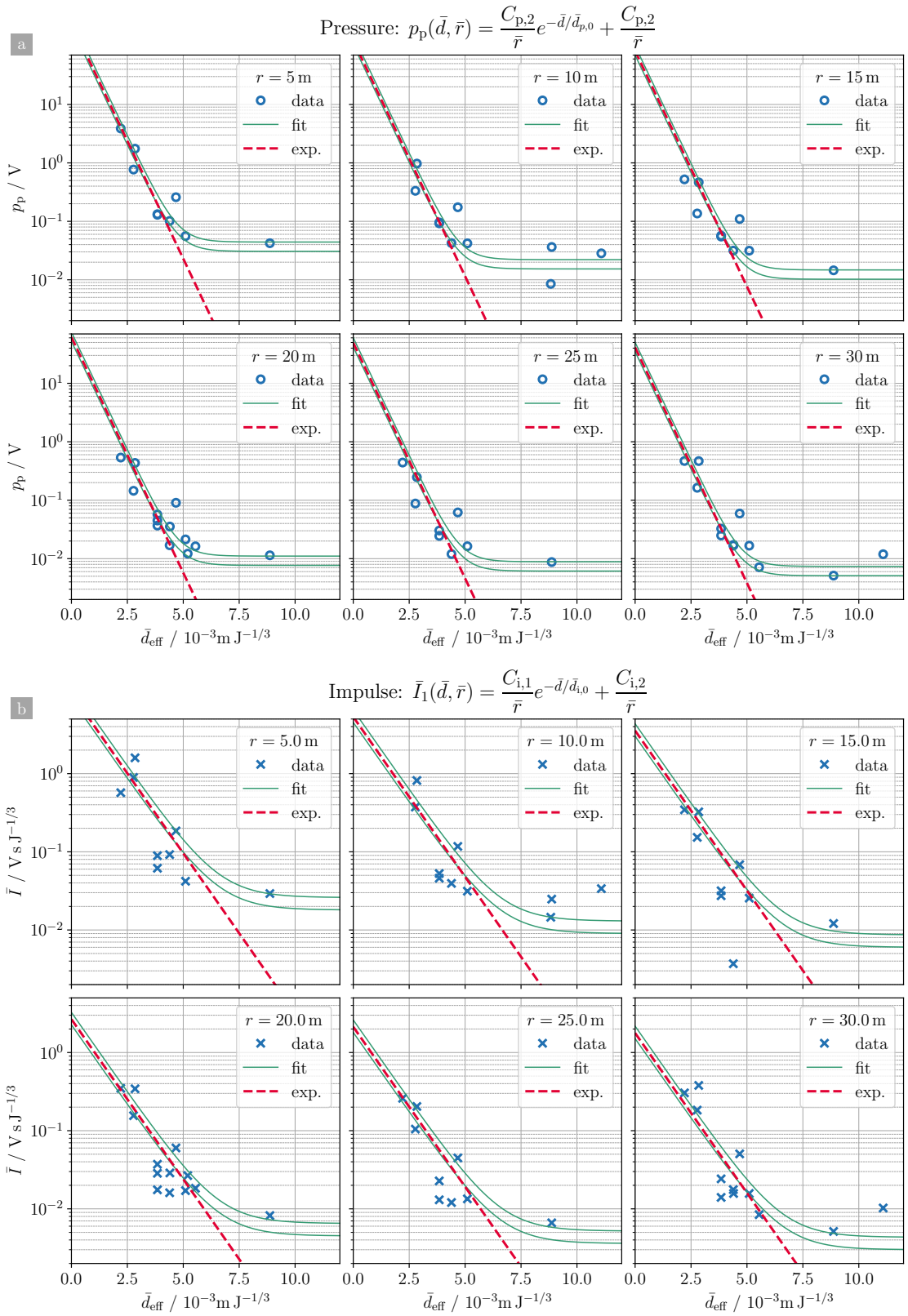

Figure 14: (*Caption on next page.*)

Figure 14: Peak pressure (**a**) and scaled impulse (**b**) of previous blast experiments, measured between 5 m and 30 m from the blasts. Pressures are shown in raw units (Volts). Depth dependencies are exponential for $\bar{d} \leq 5 \times 10^{-3}\,\mathrm{m\,J^{-1/3}}$. Peak pressure decays roughly double as fast compared to impulse ($\bar{d}_{p,0} = 5.4 \times 10^{-4}\,\mathrm{m\,J^{-1/3}}$, $\bar{d}_{i,0} = 11 \times 10^{-4}\,\mathrm{m\,J^{-1/3}}$). The red dashed lines are the exponentials $C_{\mathrm{p},1} e^{-\bar{d}/\bar{d}_{p,0}}/\bar{r}$ and $C_{\mathrm{i},1} e^{-\bar{d}/\bar{d}_{p,0}}/\bar{r}$, for pressure and impulse, respectively.

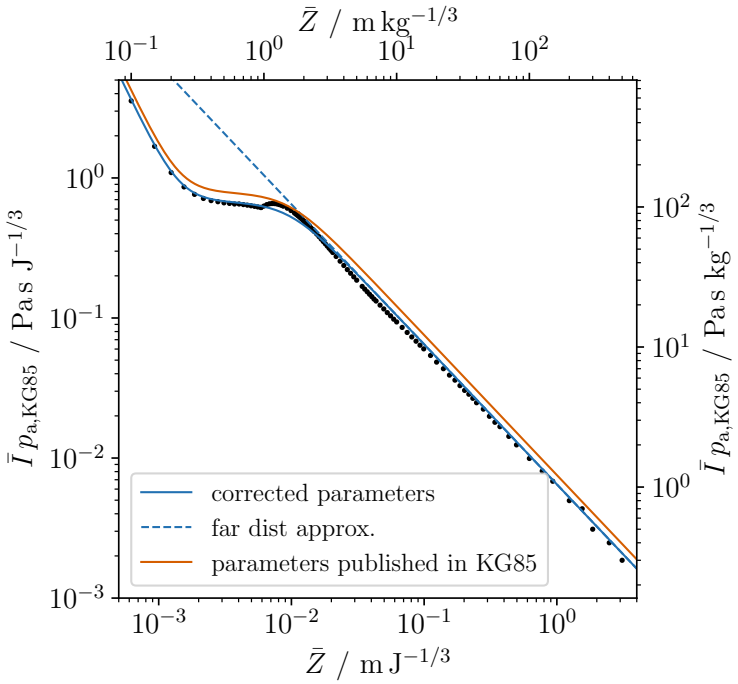

Figure 15: Effect of corrected value for $\bar{I}_0$ on the interpolation curve (Equation 29). For a reason not known to the authors the original value for $\bar{I}_0$ (orange curve) does not fit the KG85 data (black dots) well. We used a changed value, which better fits this data (blue curves, Table 5).

Overpressure:

$$\bar{p} = \bar{p}_0 \frac{1 + \left(\frac{\bar{r}}{Z_{p,0}}\right)^2}{\sqrt{1 + \left(\frac{\bar{r}}{Z_{p,1}}\right)^2}\sqrt{1 + \left(\frac{\bar{r}}{Z_{p,2}}\right)^2}\sqrt{1 + \left(\frac{\bar{r}}{Z_{p,3}}\right)^2}} \tag{28}$$

Scaled impulse:

$$\bar{I}_1 = \bar{I}_0 \frac{\sqrt{1 + \left(\frac{\bar{r}}{Z_{I,0}}\right)^4}}{\left(\frac{\bar{r}}{Z_{I,1}}\right)^2 \left(1 + \left(\frac{\bar{r}}{Z_{I,2}}\right)^3\right)^{1/3}} \tag{29}$$

Scaled blast duration:

$$\bar{t}_\mathrm{d} = \bar{t}_0 \frac{1 + \left(\frac{\bar{r}}{Z_{t,0}}\right)^{10}}{\left(1 + \left(\frac{\bar{r}}{Z_{t,1}}\right)^3\right)\left(1 + \left(\frac{\bar{r}}{Z_{t,2}}\right)^6\right)\left(1 + \left(\frac{\bar{r}}{Z_{t,3}}\right)^2\right)^{1/2}} \tag{30}$$

Values for the constants $Z_{x,y}$ are given in Table 5. For large distances, i.e. $\bar{r} \gg Z_{x,y}$ the 1 in each of the factors in the above formulas becomes small when compared to the factor $\bar{r}/Z_{x,y}$ and can be neglected. Then $\bar{p}$ and $\bar{I}$ go with $\bar{r}^{-1}$:

$$\begin{aligned} \bar{p} &\sim \bar{p}_0 \frac{Z_{p,1} Z_{p,2} Z_{p,3}}{Z_{p,0}} \frac{1}{\bar{r}} &&= \frac{a_{p,\mathrm{ref}}}{\bar{r}} \\ \bar{I} &\sim \bar{I}_0 \frac{Z_{I,1}^2 Z_{I,2}}{Z_{I,0}^2} \frac{1}{\bar{r}} &&= \frac{a_{I,\mathrm{ref}}}{\bar{r}} \end{aligned} \tag{31}$$

C Impulse Depth- and Distance Dependency

Ford et al. (2014) found the following model to fit scaled blast impulse, distance and depth:

$$\log_{10} \bar{I} = \beta_1 + \log_{10} \bar{r} + \beta_3 \bar{h} - \log_{10}(1 + 10^{10\beta_3 \bar{h}})/10 \tag{32}$$

Here $\bar{h}$ is the scaled height of burst, and energy was specified in kg TNT. Changing to scaled depth of explosion ($\bar{d} = -\bar{h}$), this can be written as

$$\bar{I}_1 = \frac{b_1}{\bar{r}} \frac{e^{-\bar{d}/\bar{d}_3}}{\left(1 + e^{-10\bar{d}/\bar{d}_3}\right)^{1/10}} \quad . \tag{33}$$

Constants b_1 and $\bar{d}_3$ are listed in Table 6. Ford et al. present the scaled impulse multiplied by ambient reference pressure, which is different from this study where scaled impulse is scaled overpressure integrated over energy-scaled time. We note that for $\bar{d} = \bar{h} = 0$ the depth dependent part reduces to $2^{-0.1} \simeq 0.93$, which is about 7% different from an exponential ($e^0 = 1$). For larger depths this

Table 5: Constants for the empirical interpolation formulas for blast pulse overpressure, scaled impulse and scaled duration, in SI and kg-TNT equivalent units.

Constant	SI	$\mathrm{kg_{TNT}}$	Remarks
		Pressure	
$\bar{p}_0$	8.08×10^2	8.08×10^2	Scaled length- and time units differ by a factor of the 1/3 power of 1 kg TNT explosive energy. $(E_{\mathrm{kg\ TNT}})^{1/3} = (4.184 \times 10^6\,\mathrm{J})^{1/3} = 161.1\,\mathrm{J}^{1/3}$.
$Z_{p,0}$	$2.79 \times 10^{-2}\,\mathrm{m\,J^{-1/3}}$	$4.50\,\mathrm{m\,kg^{-1/3}}$	
$Z_{p,1}$	$2.98 \times 10^{-4}\,\mathrm{m\,J^{-1/3}}$	$4.80\,\mathrm{m\,kg^{-1/3}}$	
$Z_{p,2}$	$1.99 \times 10^{-3}\,\mathrm{m\,J^{-1/3}}$	$0.32\,\mathrm{m\,kg^{-1/3}}$	
$Z_{p,3}$	$8.38 \times 10^{-3}\,\mathrm{m\,J^{-1/3}}$	$1.35\,\mathrm{m\,kg^{-1/3}}$	
		Impulse	
$\bar{I}_0$	$3.52 \times 10^{-7}\,\mathrm{s\,J^{-1/3}}$	$5.68 \times 10^{-5}\,\mathrm{s\,kg^{-1/3}}$	Original value for $\bar{I}_0$ from Kinney et al. (1985) is $6.61 \times 10^{-5}\,\mathrm{s\,kg^{-1/3}} = 6.7 \times 10^{-2}\,\mathrm{bar\,ms\,kg^{-1/3}}/1.01325\,\mathrm{bar}$.
$Z_{I,0}$	$1.43 \times 10^{-3}\,\mathrm{m\,J^{-1/3}}$	$0.23\,\mathrm{m\,kg^{-1/3}}$	
$Z_{I,1}$	$6.21 \times 10^{-3}\,\mathrm{m\,J^{-1/3}}$	$1.00\,\mathrm{m\,kg^{-1/3}}$	
$Z_{I,2}$	$9.62 \times 10^{-3}\,\mathrm{m\,J^{-1/3}}$	$1.55\,\mathrm{m\,kg^{-1/3}}$	
		Duration	
$\bar{t}_0$	$6.08 \times 10^{-3}\,\mathrm{s\,J^{-1/3}}$	$0.980\,\mathrm{s\,kg^{-1/3}}$	
$Z_{t,0}$	$3.35 \times 10^{-3}\,\mathrm{m\,J^{-1/3}}$	$0.54\,\mathrm{m\,kg^{-1/3}}$	
$Z_{t,1}$	$1.24 \times 10^{-3}\,\mathrm{m\,J^{-1/3}}$	$0.02\,\mathrm{m\,kg^{-1/3}}$	
$Z_{t,2}$	$4.59 \times 10^{-3}\,\mathrm{m\,J^{-1/3}}$	$0.74\,\mathrm{m\,kg^{-1/3}}$	
$Z_{t,3}$	$4.28 \times 10^{-2}\,\mathrm{m\,J^{-1/3}}$	$6.90\,\mathrm{m\,kg^{-1/3}}$	

Table 6: Constants for the empirical impulse scaling formula from Ford et al., 2014.

Constant		SI	$\mathrm{kg_{TNT}}$
β_1	$b_1 = \frac{1\,\mathrm{Pa\,s\,m}}{p_{\mathrm{a,ref}}} \times \frac{10^{\beta_1}}{E_{\mathrm{kg,TNT}}^{2/3}}$	2.48	2.48
b_1		$1.15 \times 10^{-7}\,\mathrm{s\,m\,J^{-2/3}}$	$1.85 \times 10^{-5}\,\mathrm{s\,m\,kg^{-2/3}}$
β_3	$\bar{d}_3 = \frac{1}{\beta_3 \ln 10}$	$3.46 \times 10^{2}\,\mathrm{J^{1/3}\,m^{-1}}$	$2.15\,\mathrm{kg^{1/3}\,m^{-1}}$
$\bar{d}_3$		$1.25 \times 10^{-3}\,\mathrm{m\,J^{-1/3}}$	$0.202\,\mathrm{m\,kg^{-1/3}}$
$p_{\mathrm{a,ref}}$		$1.01325 \times 10^{5}\,\mathrm{Pa}$	$1.01325 \times 10^{5}\,\mathrm{Pa}$
$E_{\mathrm{kg,TNT}}$		$4.184 \times 10^{6}\,\mathrm{J}$	$1\,\mathrm{kg}$

difference is smaller, which justifies the use of an exponential depth part (A) without the reducing factor which is necessary above the surface:

$$\bar{I} = \frac{b_1}{\bar{r}}\, e^{-\bar{d}/\bar{d}_3} \tag{34}$$

Acknowledgments

The authors acknowledge NSF grant EAR-1420455 for funding the necessary blasting resources, and University at Buffalo for hosting a workshop during which experiments were conducted. We thank Andrew Harp for his support preparing the experiments. Kayley Diem-Kay, Norman Yu and David Hyman are acknowledged for their assistance with experiment preparation and data recording.

The authors express appreciation to Kent Gee, Dept. of Physics and Astronomy at Brigham Young University (BYU) for providing the equipment used for the broadband microphone measurements in this experiment. Funding for the BYU acoustical measurement team's participation came from the BYU College of Physical and Mathematical Sciences that funded six undergraduate research assistant: Sarah Ostergaard, Eric Lynsenko, Grace McKay Smith, Christian Lopez, Carla Wallace, and Menley Hawkes; and the NSF-funded research Experience for Teachers hosted at BYU that allowed middle school science teacher Julio Escobedo to play a pivotal role.

We thank Sean Maher and Richard Sanderson for their assistance with the seismic and infrasound field instrumentation preparation and deployment. Matoza acknowledges NSF grant EAR-1847736.

Two anonymous reviewers is thanked for their thoughtful and patient comments and suggestions.

All measured data is hosted as datasets on Zenodo (Sonder, Graettinger, Neilsen, et al. 2021). Data is also available separately as listed in the supporting information document (dataset S1).

References

Ahern, T. K. and B. Dost (Aug. 1, 2012). *SEED Standard for the Exchange of Earthquake Data.* Format version 2.4. Reference Manual. Incorporated Research Institutions for Seismology (IRIS).

Ambrosini, R. D., B. M. Luccioni, R. F. Danesi, J. D. Riera, and M. M. Rocha (July 1, 2002). "Size of Craters Produced by Explosive Charges on or above the Ground Surface". In: *Shock Waves* 12.1, pp. 69–78. DOI: 10.1007/s00193-002-0136-3.

Ambrosini, R. D. and B. M. Luccioni (2006). "Craters Produced by Explosions on the Soil Surface". In: *Journal of Applied Mechanics* 73.6, p. 890. DOI: 10.1115/1.2173283.

Antoun, T. H., I. N. Lomov, and L. A. Glenn (Dec. 2003). "Simulation of the Penetration of a Sequence of Bombs into Granitic Rock". In: *International Journal of Impact Engineering* 29.1-10, pp. 81–94.

Arora, H., P. Del Linz, and J. Dear (June 2017). "Damage and Deformation in Composite Sandwich Panels Exposed to Multiple and Single Explosive Blasts". In: *International Journal of Impact Engineering* 104, pp. 95–106. DOI: 10.1016/j.ijimpeng.2017.01.017.

Boatwright, J. (1980). "A Spectral Theory for Circular Seismic Sources; Simple Estimates of Source Dimension, Dynamic Stress Drop, and Radiated Seismic Energy". In: *Bulletin of the Seismological Society of America* 70.1, pp. 1–27.

Bowman, D. C., J. Taddeucci, K. Kim, J. F. Anderson, J. M. Lees, A. H. Graettinger, I. Sonder, and G. A. Valentine (2014). "The Acoustic Signatures of Ground Acceleration, Gas Expansion, and Spall Fallback in Experimental Volcanic Explosions". In: *Geophysical Research Letters* 41.6, pp. 1916–1922. DOI: 10.1002/2014GL059324.

Bush, V., J. P. Conant, and E. B. J. Wilson (1946). *Effects of Impact and Explosion*. Technical report AD0221586. Washington DC: Office of Scientific Research and Development, p. 506.

Büttner, R. and B. Zimanowski (1998). "Physics of Thermohydraulic Explosions." In: *Physical Review E* 57.5, pp. 5726–5729. DOI: 10.1103/PhysRevE.57.5726.

Cashman, K. V. and B. Scheu (2015). "Magmatic Fragmentation". In: *The Encyclopedia of Volcanoes*. Elsevier, pp. 459–471. DOI: 10.1016/B978-0-12-385938-9.00025-0.

Crighton, D. G. and J. F. Scott (Aug. 24, 1979). "Asymptotic Solutions of Model Equations in Nonlinear Acoustics". In: *Philosophical Transactions of the Royal Society of London. Series A, Mathematical and Physical Sciences* 292.1389, pp. 101–134. DOI: 10.1098/rsta.1979.0046.

Dillon, L. A. (1972). *The Influence of Soil and Rock Properties on the Dimensions of Explosion-Produced Craters*. Technical report AD0891964. New Mexico: Air Force Weapons Laboratory, Air Force Systems Command Kirtland Air Force Base, p. 172.

Dürig, T., M. Gudmundsson, and P. Dellino (2015). "Reconstruction of the Geometry of Volcanic Vents by Trajectory Tracking of Fast Ejecta - the Case of the Eyjafjallajokull 2010 Eruption (Iceland)". In: *Earth, Planets and Space* 67.1, p. 64. DOI: 10.1186/s40623-015-0243-x.

Dürig, T., M. T. Gudmundsson, S. Karmann, B. Zimanowski, P. Dellino, M. Rietze, and R. Büttner (2015). "Mass Eruption Rates in Pulsating Eruptions Estimated from Video Analysis of the Gas Thrust-Buoyancy Transition—a Case Study of the 2010 Eruption of Eyjafjallajökull, Iceland". In: *Earth, Planets and Space* 67.1, pp. 1–17. DOI: 10.1186/s40623-015-0351-7.

Dürig, T., P.-S. Ross, P. Dellino, J. D. L. White, D. Mele, and P. P. Comida (Nov. 2021). "A Review of Statistical Tools for Morphometric Analysis of Juvenile Pyroclasts". In: *Bulletin of Volcanology* 83.11, p. 79. DOI: 10.1007/s00445-021-01500-0.

Ehrgott John Q., J., S. A. Akers, J. E. Windham, D. D. Rickman, and K. T. Danielson (2011). "The Influence of Soil Parameters on the Impulse and Airblast Overpressure Loading above Surface-Laid and Shallow-Buried Explosives". In: *Shock and Vibration* 18.6. DOI: 10.3233/SAV-2010-0609.

Fee, D., R. Waxler, J. Assink, Y. Gitterman, J. Given, J. Coyne, P. Mialle, M. Garces, D. Drob, D. Kleinert, R. Hofstetter, and P. Grenard (June 27, 2013). "Overview of the 2009 and 2011 Sayarim Infrasound Calibration Experiments: Sayarim Infrasound Overview". In: *Journal of Geophysical Research: Atmospheres* 118.12, pp. 6122–6143. DOI: 10.1002/jgrd.50398.

Ford, S. R., A. J. Rodgers, H. Xu, D. C. Templeton, P. Harben, W. Foxall, and R. E. Reinke (Mar. 25, 2014). "Partitioning of Seismoacoustic Energy and Estimation of Yield and Height-of-Burst/Depth-of-Burial for near-Surface Explosions". In: *Bulletin of the Seismological Society of America* 104.2, pp. 608–623. DOI: 10.1785/0120130130.

Garces, M. (Oct. 2018). "Explosion Source Models". In: *Infrasound Monitoring for Atmospheric Studies*. Springer International Publishing, pp. 273–345. DOI: 10.1007/978-3-319-75140-5_8.

Garcés, M. A., D. Fee, and R. S. Matoza (2013). *Modeling Volcanic Processes: The Physics and Mathematics of Volcanism*. Ed. by S. A. Fagents, T. K. P. Gregg, and R. M. C. Lopes. Cambridge: Cambridge University Press. DOI: 10.1017/CBO9781139021562.

Gaudin, D., J. Taddeucci, B. F. Houghton, T. R. Orr, D. Andronico, E. D. Bello, U. Kueppers, T. Ricci, and P. Scarlato (Oct. 2016). "3-D High-Speed Imaging of Volcanic Bomb Trajectory in Basaltic Explosive Eruptions". In: *Geochemistry, Geophysics, Geosystems* 17.10, pp. 4268–4275. DOI: 10.1002/2016gc006560.

Gonnermann, H. M. and M. Manga (2007). "The Fluid Mechanics inside a Volcano". In: *Annual Review of Fluid Mechanics* 39, pp. 321–356. DOI: 10.1146/annurev.fluid.39.050905.110207.

Goto, A., M. Ripepe, and G. Lacanna (June 16, 2014). "Wideband Acoustic Records of Explosive Volcanic Eruptions at Stromboli: New Insights on the Explosive Process and the Acoustic Source: Goto et al.: Wideband Acoustic Records of Stromboli". In: *Geophysical Research Letters* 41.11, pp. 3851–3857. DOI: 10.1002/2014GL060143.

Goto, A., H. Taniguchi, M. Yoshida, T. Ohba, and H. Oshima (2001). "Effects of Explosion Energy and Depth to the Formation of Blast Wave and Crater: Field Explosion Experiment for the Understanding of Volcanic Explosion". In: *Geophysical Research Letters* 28.22, pp. 4287–4290. DOI: 10.1029/2001GL013213.

Grady, D. E. (1996). "Shock-Wave Properties of Brittle Solids". In: *AIP Conference Proceedings*. Proceedings of the Conference of the American Physical Society Topical Group on Shock Compression of Condensed Matter. Vol. 370. Seattle, Washington (USA): AIP, pp. 9–20. DOI: 10.1063/1.50579.

Graettinger, A. H., G. A. Valentine, I. Sonder, P.-S. Ross, and J. D. L. White (2015). "Facies Distribution of Ejecta in Analog Tephra Rings from Experiments with Single and Multiple Subsurface Explosions". In: *Bulletin of Volcanology* 77.8, pp. 1–12. DOI: 10.1007/s00445-015-0951-x.

Graettinger, A. H., G. A. Valentine, I. Sonder, P.-S. Ross, J. D. L. White, and J. Taddeucci (2014). "Maar-Diatreme Geometry and Deposits: Subsurface Blast Experiments with Variable Explosion Depth". In: *Geochem. Geophys. Geosys.* 15.3, pp. 740–764. DOI: 10.1002/2013GC005198.

Graettinger, A. H., G. A. Valentine, and I. Sonder (2015). "Circum-Crater Variability of Deposits from Discrete, Laterally and Vertically Migrating Volcanic Explosions: Experimental Evidence and Field Implications". In: *Journal of Volcanology and Geothermal Research* 308, pp. 61–69. DOI: 10.1016/j.jvolgeores.2015.10.019.

Guzas, E. L. and C. J. Earls (Aug. 25, 2010). "Air Blast Load Generation for Simulating Structural Response". In: *Steel and Composite Structures* 10.5, pp. 429–455.

Hoek, E. (Feb. 1999). "Putting Numbers to Geology— an Engineer's Viewpoint". In: *Quarterly Journal of Engineering Geology and Hydrogeology* 32.1, pp. 1–19. DOI: 10.1144/gsl.qjeg.1999.032.p1.01.

Holsapple, K. A. and R. M. Schmidt (1980). "On the Scaling of Crater Dimensions: 1. Explosive Processes". In: *Journal of Geophysical Research* 85.B12, pp. 7247–7256. DOI: 10.1029/JB085iB12p07247.

Houghton, B. (2015). "Explosive Volcanism". In: *The Encyclopedia of Volcanoes*. Ed. by H. Sigurdsson, B. Houghton, S. R. McNutt, H. Rymer, and J. Stix. 2nd ed. .IV. Elsevier LTD, Oxford, pp. 457–686.

Ichihara, M., M. Ripepe, A. Goto, H. Oshima, H. Aoyama, M. Iguchi, K. Tanaka, and H. Taniguchi (Mar. 26, 2009). "Airwaves Generated by an Underwater Explosion: Implications for Volcanic Infrasound". In: *Journal of Geophysical Research* 114.B3, B03210. DOI: 10.1029/2008JB005792.

Johnson, J. and R. Aster (Dec. 2005). "Relative Partitioning of Acoustic and Seismic Energy during Strombolian Eruptions". In: *Journal of Volcanology and Geothermal Research* 148.3-4, pp. 334–354. DOI: 10.1016/j.jvolgeores.2005.05.002.

Kim, K. and A. Rodgers (July 2016). "Waveform Inversion of Acoustic Waves for Explosion Yield Estimation". In: *Geophysical Research Letters* 43.13, pp. 6883–6890. DOI: 10.1002/2016gl069624.

Kim, K. and A. Rodgers (Aug. 2017). "Influence of Low-Altitude Meteorological Conditions on Local Infrasound Propagation Investigated by 3-D Full-Waveform Modeling". In: *Geophysical Journal International* 210.2, pp. 1252–1263. DOI: 10.1093/gji/ggx218.

Kinney, G. F. and K. J. Graham (1985). *Explosive Shocks in Air*. Springer.

Lamb, F. K., B. W. Callen, and J. D. Sullivan (Jan. 1, 1991). "Yield Estimation Using Shock Wave Methods". In: *Explosion Source Phenomenology*. Ed. by S. R. Taylor, H. J. Patton, and P. G. Richards. Vol. 65. American Geophysical Union, pp. 73–89. DOI: 10.1029/GM065p0073.

Lee, C. K. B. and T. A. Mazzola (1989). "Ejecta Scaling Laws for Craters in Dry Alluvial Sites". In: *Journal of Geophysical Research: Solid Earth* 94.B12, pp. 17595–17605. DOI: 10.1029/JB094iB12p17595.

Liu, T., B. Cao, X. Liu, T.-P. Sun, and X. Cheng (2020). "Explosion Cratering in 3D Granular Media". In: *Soft Matter* 16.5, pp. 1323–1332. DOI: 10.1039/C9SM01688K.

Lorenz, V. (1975). "Formation of Phreatomagmatic Maar-Diatreme Volcanoes and Its Relevance to Kimberlite Diatremes". In: *Physics and Chemistry of the Earth* 9.0, pp. 17–27. DOI: 10.1016/0079-1946(75)90003-8.

Macorps, É., A. H. Graettinger, G. A. Valentine, P.-S. Ross, J. D. L. White, and I. Sonder (Mar. 2016). "The Effects of the Host-Substrate Properties on Maar-Diatreme Volcanoes: Experimental Evidence". In: *Bulletin of Volcanology* 78.4. DOI: 10.1007/s00445-016-1013-8.

Maher, S. P., R. S. Matoza, C. D. Groot-Hedlin, K. L. Gee, D. Fee, and A. Yokoo (Mar. 2020). "Investigating Spectral Distortion of Local Volcano Infrasound by Nonlinear Propagation at Sakurajima Volcano, Japan". In: *Journal of Geophysical Research: Solid Earth* 125.3. DOI: 10.1029/2019JB018284.

Mammadova, N., S. Ghaisas, G. Zenitsky, D. S. Sakaguchi, A. G. Kanthasamy, J. J. Greenlee, and M. H. West Greenlee (July 2017). "Lasting Retinal Injury in a Mouse Model of Blast-Induced Trauma". In: *The American Journal of Pathology* 187.7, pp. 1459–1472. DOI: 10.1016/j.ajpath.2017.03.005.

Marchetti, E., M. Ripepe, D. Delle Donne, R. Genco, A. Finizola, and E. Garaebiti (Nov. 28, 2013). "Blast Waves from Violent Explosive Activity at Yasur Volcano, Vanuatu". In: *Geophysical Research Letters* 40.22, pp. 5838–5843. DOI: 10.1002/2013GL057900.

Matoza, R. S., D. Fee, and T. M. Lopez (Nov. 1, 2014). "Acoustic Characterization of Explosion Complexity at Sakurajima, Karymsky, and Tungurahua Volcanoes". In: *Seismological Research Letters* 85.6, pp. 1187–1199. DOI: 10.1785/0220140110.

Matoza, R. S., A. Arciniega-Ceballos, R. W. Sanderson, G. Mendo-Pérez, A. Rosado-Fuentes, and B. A. Chouet (Jan. 2019). "High-Broadband Seismoacoustic Signature of Vulcanian Explosions at Popocatépetl Volcano, Mexico". In: *Geophysical Research Letters* 46.1, pp. 148–157. DOI: 10.1029/2018gl080802.

Matoza, R. S., M. A. Garcés, B. A. Chouet, L. D'Auria, M. A. H. Hedlin, C. De Groot-Hedlin, and G. P. Waite (Apr. 24, 2009). "The Source of Infrasound Associated with Long-period Events at Mount St. Helens". In: *Journal of Geophysical Research* 114.B4, B04305. DOI: 10.1029/2008JB006128.

Muhlestein, M. B., K. L. Gee, and J. H. Macedone (Mar. 2012). "Educational Demonstration of a Spherically Propagating Acoustic Shock". In: *The Journal of the Acoustical Society of America* 131.3, pp. 2422–2430. DOI: 10.1121/1.3676730.

Nordyke, M. D. (1961). "Nuclear Craters and Preliminary Theory of the Mechanics of Explosive Crater Formation". In: *Journal of Geophysical Research* 66.10, pp. 3439–3459. DOI: 10.1029/JZ066i010p03439.

Ohba, T., H. Taniguchi, H. Oshima, M. Yoshida, and A. Goto (June 2002). "Effect of Explosion Energy and Depth on the Nature of Explosion Cloud". In: *Journal of Volcanology and Geothermal Research* 115.1-2, pp. 33–42. DOI: 10.1016/s0377-0273(01)00307-9.

Ouchterlony, F. and J. Sanchidrián (Oct. 2019). "A Review of Development of Better Prediction Equations for Blast Fragmentation". In: *Journal of Rock Mechanics and Geotechnical Engineering* 11.5, pp. 1094–1109. DOI: 10.1016/j.jrmge.2019.03.001.

Park, I., A. Jolly, R. S. Matoza, B. Kennedy, G. Kilgour, R. Johnson, E. Garaebiti, and S. Cevuard (Sept. 2021). "Seismo-Acoustic Characterisation of the 2018 Ambae (Manaro Voui) Eruption, Vanuatu". In: *Bulletin of Volcanology* 83.9, p. 60. DOI: 10.1007/s00445-021-01474-z.

Pistolesi, M., D. Delle Donne, L. Pioli, M. Rosi, and M. Ripepe (2011). "The 15 March 2007 Explosive Crisis at Stromboli Volcano, Italy: Assessing Physical Parameters through a Multidisciplinary Approach". In: *Journal of Geophysical Research: Solid Earth* 116.B12. DOI: 10.1029/2011JB008527.

Qiu, X., X. Shi, Y. Gou, J. Zhou, H. Chen, and X. Huo (Apr. 2018). "Short-Delay Blasting with Single Free Surface: Results of Experimental Tests". In: *Tunnelling and Underground Space Technology* 74, pp. 119–130. DOI: 10.1016/j.tust.2018.01.014.

Rickman, D. D., J. Richard G. Rhett, S. A. Akers, I. Jim W. Hall, and J. E. Windham (2011). *An Evaluation of the Effect of Soil Parameters on Explosive Cratering: Results and Analyses of Intermediate-Scale Tests*. ERDC/GSL TR-11-38. US Army Corps of Engineers Engineer Research and Development Center.

Rocco, J. R. and J. M. Thomsen (2010). "The Nuclear Retarc Sulky: An Upside down Crater". In: *Military Aspects of Blast and Shock (MABS 21) Conference Proceedings*. ADA560596. Defense Threat Reduction Agency.

Rogers, P. H. (1977). "Weak-Shock Solution for Underwater Explosive Shock Waves". In: *The Journal of the Acoustical Society of America* 62.6, p. 1412. DOI: 10.1121/1.381674.

Ross, P.-S., J. D. L. White, G. A. Valentine, J. Taddeucci, I. Sonder, and R. G. Andrews (2013). "Experimental Birth of a Maar-Diatreme Volcano". In: *Journal of Volcanology and Geothermal Research* 260, pp. 1–12. DOI: 10.1016/j.jvolgeores.2013.05.005.

Sato, H. and H. Taniguchi (1997). "Relationship between Crater Size and Ejecta Volume of Recent Magmatic and Phreato-Magmatic Eruptions: Implications for Energy Partitioning - Range". In: *Geophysical Research Letters* 24.3, pp. 205–208. DOI: 10.1029/96GL04004.

Schnurr, J., K. Kim, M. A. Garces, and A. Rodgers (May 1, 2020). "Improved Parametric Models for Explosion Pressure Signals Derived From Large Datasets". In: *Seismological Research Letters* 91.3, pp. 1752–1762. DOI: 10.1785/0220190278.

Sonder, I., A. H. Graettinger, and G. A. Valentine (2015). "Scaling Multiblast Craters: General Approach and Application to Volcanic Craters". In: *Journal of Geophysical Research, Solid Earth* 120.9, pp. 6141–6158. DOI: 10.1002/2015JB012018.

Sonder, I., A. H. Graettinger, T. B. Neilsen, R. S. Matoza, J. Taddeucci, J. Oppenheimer, E. Lev, K. Tsunematsu, G. P. Waite, G. A. Valentine, and K. Befus (Aug. 31, 2021). *2018 NSF Large Scale Experiment Workshop on Volcanic Blasts*. Version 0.5. Zenodo. DOI: 10.5281/ZENODO.5879934.

Strange, J. N., C. W. Denzel, and T. I. McLane III (1960). *Cratering from High Explosive Charges. Analysis of Crater Data*. AD0263170. Vicksburg, MS: Army Engineer Waterways Experiment Station.

Taddeucci, J., J. J. Peña Fernández, V. Cigala, U. Kueppers, P. Scarlato, E. Del Bello, T. Ricci, J. Sesterhenn, and S. Panunzi (Aug. 2021). "Volcanic Vortex Rings: Axial Dynamics, Acoustic

Features, and Their Link to Vent Diameter and Supersonic Jet Flow". In: *Geophysical Research Letters* 48.15. DOI: 10.1029/2021GL092899.

Taddeucci, J., G. Sottili, D. Palladino, G. Ventura, and P. Scarlato (2010). "A Note on Maar Eruption Energetics: Current Models and Their Application". In: *Bulletin of Volcanology* 72.1, pp. 75–83. DOI: 10.1007/s00445-009-0298-2.

Taylor, Z. J., R. Gurka, G. A. Kopp, and A. Liberzon (2010). "Long-Duration Time-Resolved PIV to Study Unsteady Aerodynamics". In: *IEEE Transactions on Instrumentation and Measurement* 59.12, pp. 3262–3269. DOI: 10.1109/TIM.2010.2047149.

Valentine, G. A., A. H. Graettinger, É. Macorps, P.-S. Ross, J. D. L. White, É. Döhring, and I. Sonder (2015). "Experiments with Vertically and Laterally Migrating Subsurface Explosions with Applications to the Geology of Phreatomagmatic and Hydrothermal Explosion Craters and Diatremes". In: *Bulletin of Volcanology* 77.3, 15. DOI: 10.1007/s00445-015-0901-7.

Valentine, G. A., A. H. Graettinger, and I. Sonder (2014). "Explosion Depths for Phreatomagmatic Eruptions". In: *Geophysical Research Letters* 41.9, pp. 3045–3051. DOI: 10.1002/2014GL060096.

Valentine, G. A., J. D. L. White, P.-S. Ross, J. Amin, J. Taddeucci, I. Sonder, and P. J. Johnson (2012). "Experimental Craters Formed by Single and Multiple Buried Explosions and Implications for Maar-Diatreme Volcanoes". In: *Geophysical Research Letters* 39, p. L20301. DOI: 10.1029/2012GL053716.

Voight, B. (1981). "Time Scale for the First Moments of the May 18 Eruption". In: *Geological Survey Professional Paper*. 1250. Vol. 1250: *The 1980 Eruptions of Mount St. Helens, Washington*. Ed. by P. W. Lipman and D. R. Mullineaux. Geological Survey Professional Paper. U.S. Government Printing Office, pp. 69–93.

Vortman, L. J. (1968). "Craters from Surface Explosions and Scaling Laws". In: *Journal of Geophysical Research* 73.14, pp. 4621–4636. DOI: 10.1029/JB073i014p04621.

Yokoo, A., H. Taniguchi, A. Goto, and H. Oshima (Dec. 2002). "Energy and Depth of Usu 2000 Phreatic Explosions: ENERGY AND DEPTH OF USU EXPLOSIONS". In: *Geophysical Research Letters* 29.24, pp. 48-1-48–4. DOI: 10.1029/2002GL015928.

Young, S. M., K. L. Gee, T. B. Neilsen, and K. M. Leete (Sept. 2015). "Outdoor Measurements of Spherical Acoustic Shock Decay". In: *The Journal of the Acoustical Society of America* 138.3, EL305–EL310. DOI: 10.1121/1.4929928.

Zhou, J., W. Lu, P. Yan, M. Chen, and G. Wang (Oct. 2016). "Frequency-Dependent Attenuation of Blasting Vibration Waves". In: *Rock Mechanics and Rock Engineering* 49.10, pp. 4061–4072. DOI: 10.1007/s00603-016-1046-5.

Zimanowski, B., R. Büttner, P. Dellino, J. D. L. White, and K. H. Wohletz (2015). "Magma–Water Interaction and Phreatomagmatic Fragmentation". In: *The Encyclopedia of Volcanoes*. Ed. by H. Sigurdsson, B. Houghton, H. Rymer, J. Stix, and S. McNutt. 2nd ed. Elsevier. Chap. 26, pp. 473–484. DOI: 10.1016/b978-0-12-385938-9.00026-2.

Zimanowski, B., K. H. Wohletz, P. Dellino, and R. Büttner (2003). "The Volcanic Ash Problem". In: *Journal of Volcanology and Geothermal Research* 122.1-2, pp. 1–5. DOI: 10.1016/S0377-0273(02)00471-7.